Journal of Energy Chemistry 116 (2026) 322–338

Contents lists available at ScienceDirect

Journal of Energy Chemistry

journal homepage: www.elsevier.com/locate/jechem

http://www.journals.elsevier.com/journal-of-energy-chemistry/

# Thermocatalytic $CO_2$ hydrogenation to high-yield ethanol and $C_3$ $C_5$ alcohols over promoted Fe-based catalysts ☆

Andrii Kostyniuk *, Stanislav Yakushkin, Blaž Likozar

*Department of Catalysis and Chemical Reaction Engineering, National Institute of Chemistry, Hajdrihova 19, Ljubljana 1001, Slovenia*

ARTICLE INFO

*Article history:*
Received 24 November 2025
Revised 25 December 2025
Accepted 2 January 2026
Available online 14 January 2026

*Keywords:*
$CO_2$ hydrogenation
Rb/CuZnFe heterogeneous catalyst
C–C coupling
Ethanol and higher alcohols synthesis

ABSTRACT

Direct catalytic hydrogenation is an effective approach for $CO_2$ utilization to produce ethanol and higher alcohols (HA), but developing non-precious metal catalysts with high activity and selectivity remains a major challenge. In this study, we report the development of a highly efficient 4 wt%Rb/25 wt%Cu-25 wt%Zn-50 wt%Fe catalyst, synthesized via the co-precipitation method, for the selective hydrogenation of $CO_2$ to ethanol and HA in a continuous flow fixed-bed reactor. The catalyst delivers an ethanol space-time yield (STY) of 4.4 mmol $g_{cat}^{-1}$ $h^{-1}$ with 48.8% ethanol selectivity in the gas phase, while the condensed liquid fraction exhibits a maximum $C_{2+}OH$ selectivity of 85.3% under 20 bar ($H_2/CO_2$ = 3) in the temperature range of 200–300 °C over 16–19 h. The superior catalytic performance is attributed to the optimized Rb loading, which enhances structural stability, preserves crystallinity, and mitigates Cu leaching. The Rb-promoting effect on C–C coupling arises from the synergistic interactions among Rb-Cu-Fe, as well as Rb-Cu-Zn. This synergy facilitates the formation of $CH_3CH_2O^*$, $CH_3COO^*$, and $CH_3CHO^*$ species on Rb/Cu-$Fe_5C_2$ and Rb/CuZn sites. Notably, the 4%Rb/CuZnFe catalyst exhibits the most significant modifications in its electronic environment, likely due to changes in oxygen vacancies and altered metal-oxygen interactions upon Rb incorporation. Furthermore, the 4% Rb content plays a critical role in maintaining an optimal balance between catalyst basicity and oxygen vacancies, effectively enhancing $CO_2$ activation while suppressing side reactions. These findings underscore the potential of Rb-modified CuZnFe catalysts for efficient $CO_2$ hydrogenation to HA, offering a promising avenue for sustainable chemical production.



## 1. Introduction

The burning of fossil fuels such as coal, oil, and natural gas releases massive amounts of $CO_2$ into the atmosphere, driving global warming, disrupting weather patterns, accelerating glacier melt, and raising sea levels, highlighting the urgent need for effective emission reduction strategies [1,2]. One promising approach is converting waste $CO_2$ into value-added chemicals using renewable energy and $H_2$, which can both recycle $CO_2$ and reduce dependence on fossil resources [3]. The production of high-value-added multicarbon ($C_{2+}$) products is highly desirable for practical applications, but remains a significant challenge, with ethanol standing out due to its high energy density (26.8 MJ $kg^{-1}$) and ease of transport and storage [4].

Ethanol (EtOH) plays a multifaceted role as a clean transportation fuel, fuel additive, promising hydrogen carrier, industrial intermediate, solvent, and low-temperature liquid. Global bioethanol production continues to grow steadily, driven primarily by expanding demand in major producing regions. Brazil remains the dominant contributor to this increase, followed by notable growth in emerging producers such as Thailand, China, India, and the Philippines [5]. The conventional route for EtOH production relies on the fermentation of cellulosic biomass. This route is unsustainable to satisfy the increasing EtOH demand, particularly for the practical utilization as a gasoline additive, making nature cannot provide fuel and food for such a world with a growing population [6].

Numerous catalytic systems have been explored for $CO_2$ hydrogenation to EtOH, with noble-metal catalysts like Ir, Rh, Ru, Pt, and Pd commonly used to enhance C–O bond activation and C–C

☆ This article is part of a special issue entitled: 'ICEC2025' published in Journal of Energy Chemistry.

* Corresponding author.
*E-mail address:* andrii.kostyniuk@ki.si (A. Kostyniuk).

https://doi.org/10.1016/j.jechem.2026.01.005

coupling [7–13]. However, due to the high cost of noble metals, research has shifted towards more affordable 3*d* transition metal catalysts, such as Cu, Fe, Zn, and Co, with Cu-Fe, Zn-Fe, Cu-Co, and Cu-Zn-Fe catalysts emerging as a particularly effective and economical option for producing higher alcohols (HA) from $CO_2$ [14–22]. Additionally, the role of each element in these catalysts is not well understood, and further improvements are vital for developing industrially viable reaction processes.

Moreover, very recently, several research groups, including our own [9,14,15,17,18,23–25], have investigated the promotional effect of alkali elements on bi- and trimetallic oxide catalysts to enhance their efficiency for ethanol production from $CO_2$. Alkali metals, such as Cs, Na, and K, have been reported to influence catalyst properties by modifying the electronic structure, altering metal-support interactions, and tuning the acid-base characteristics of the active sites. These modifications play a crucial role in improving ethanol selectivity while suppressing undesired byproducts. For instance, Xiang et al. [23] demonstrated that K loading significantly influences $CO_2$ hydrogenation over *x*K/FeCuAl catalysts by modulating product selectivity, where moderate K loading (1.6 wt%) maximized ethanol production (space-time yield (STY) = 603 $g_{AcH}$ $kg_{cat}^{-1}$ $h^{-1}$) via oxygenate intermediate hydrogenation, while higher K loading (3.5 wt%) favoured $C_{5+}$ hydrocarbon formation by promoting carbon chain growth, with advanced characterization revealing that K alters the catalyst electronic structure and surface basicity to govern distinct reaction pathways. Zhou et al. [18] achieved an improvement in $CO_2$ hydrogenation to $C_{2+}$ alcohols by modifying CuFeZn catalysts with $K_3PO_4$, resulting in a HA selectivity of 15.8% at 38.1% $CO_2$ conversion and a $STY_{C2+OH}$ of 53.8 mg $mL^{-1}$ $h^{-1}$, driven by optimized proportions of $Fe^{2+}$, $Cu^0$, and $Cu^+$ species which enhance C–C coupling and catalyst stability. In a notable advancement, Xu et al. [15] introduced a Cs-promoted Cu-Fe-Zn catalyst that achieved a $C_{2+}$ alcohols STY of 73.4 mg $g_{cat}^{-1}$-$h^{-1}$, with the success attributed to the synergistic interaction of Cs, Cu-ZnO, and Cu-$Fe_7C_3$, though further optimization is needed for large-scale application. Zhang et al. [24] developed a 2%Na-Co/$SiO_2$ catalyst that produced an EtOH with STY of 1.1 mmol $g^{-1}$ $h^{-1}$ and a $C_{2+}$OH/ROH fraction of 91.3%, highlighting the critical role of alkali promotion in steering product distribution. Furthermore, Xu et al. [17] demonstrated the catalytic activity of K-promoted Cu-Fe-based catalysts, with STY of 1.5 mmol $g_{cat}^{-1}$ $h^{-1}$, respectively, with K balancing CO and $H_2$ activation for effective $CH_x$–CO coupling.

However, the pursuit of highly efficient $CO_2$ conversion remains a challenge, grappling with issues such as low EtOH selectivity, productivity, and the insufficient stability of catalysts. Moreover, the direct conversion of $CO_2$ to EtOH, a more intricate process compared to multi-step reactions, continues to demonstrate unsatisfactory EtOH productivity. The disappointing yield and suboptimal selectivity observed with both transition-metal-based and noble-metal-based catalysts have ignited a search for novel strategies in $CO_2$ hydrogenation for EtOH synthesis [26].

In this work, we introduce a highly effective catalytic system, xRb/CuZnFe, which significantly boosts the EtOH and $C_{2+}$OH production rate through $CO_2$ hydrogenation. Under the optimal reaction conditions ($H_2/CO_2$ = 3; pressure (*P*) = 20 bar; gas hourly space velocity (GHSV) = 9917 $h^{-1}$; time on stream (TOS) = 16–19 h; temperature (*T*) = 300 °C), the 4 wt%Rb/25 wt%Cu-25 wt%Zn-50 wt%Fe catalyst delivers an exceptional ethanol STY of 4.4 mmol $g_{cat}^{-1}$ $h^{-1}$, accompanied by 48.8% ethanol selectivity in the gas phase and up to 85.3% $C_{2+}$OH selectivity in the liquid phase. Such performance clearly outperforms most state-of-the-art $CO_2$ hydrogenation catalysts reported to date (Fig. 1 and Table S1) [14–21,27–32]. Selectivity values shown in Fig. 1 were extracted directly from the original publications. In most cases, selectivity is reported for EtOH and/or $C_{2+}$OH, excluding CO. When CO was included in the original source, this was kept unchanged to avoid altering published data. As a result, some literature points may appear lower due to the inclusion of CO in the product distribution. To gain a deeper understanding of the catalytic mechanism, we conducted a comprehensive investigation into the role of each component in xRb/CuZnFe. A range of advanced spectroscopic techniques and physicochemical characterizations were employed. The results demonstrate that the incorporation of Rb plays a crucial role in modifying the electronic environment of Cu and Zn species and enhancing $CO_2$ adsorption and activation, while simultaneously suppressing methanation side reactions. The synergistic interaction between Rb/Cu-$Fe_5C_2$ species and Rb/CuZn alloy sites promotes C–C coupling pathways, facilitating the selective formation of ethanol and HA.

The mechanistic role of the Rb promoter differs from that of Cs reported in the literature [15,25]. Cs-modified CuZnFe catalysts have been shown to stabilize a Cu-$Fe_7C_3$ interface, which promotes CO insertion and chain propagation, leading to larger fractions of $C_3$–$C_5$ alcohols and heavier hydrocarbons. In contrast, Rb induces a moderate increase in surface basicity and oxygen vacancies, without over-stabilizing $CO_2$-derived intermediates. As a result, the Rb/CuZnFe catalyst selectively stabilizes $C_2$ intermediates ($CH_3CH_2O^*$, $CH_3COO^*$, and $CH_3CHO^*$), as evidenced by diffuse reflectance infrared Fourier transform spectroscopy (DRIFTS) spectra, and ethanol becomes the dominant oxygenate with suppressed chain growth. This balanced interfacial structure explains the high ethanol selectivity and low formation of long-chain products observed in this work.

## 2. Experimental

Details of the experimental procedures, including Materials, Sample preparation, Catalyst characterization, and Catalytic evaluation (Fig. S1), are provided in Supporting Information.

## 3. Results and discussion

### 3.1. Catalytic performance

#### 3.1.1. The effect of Rb loading, ZSM-5 support, reaction time, and temperature on the composition of the gas product

The catalytic performance of CuZnFe and *x*Rb/CuZnFe catalysts in the hydrogenation of $CO_2$ was evaluated (Fig. 2) in terms of $CO_2$ conversion, STY of $C_{2+}$ alcohols or EtOH, selectivity towards $C_{2+}$ alcohols and/or EtOH, and methyl alcohol (MeOH) selectivity in the gas phase. As shown in Fig. 2(a), at 200 °C, all catalysts exhibited low $CO_2$ conversion, ranging from ~1% to 3%. The unmodified CuZnFe and CuZnFe/ZSM-5 catalysts showed minimal activity, whereas Rb-modified CuZnFe catalysts demonstrated slightly higher conversion. Increasing the temperature to 250 °C resulted in a noticeable enhancement in $CO_2$ conversion, reaching 4%–7% for CuZnFe and CuZnFe/ZSM-5, respectively.

Notably, the *x*Rb/CuZnFe catalysts displayed higher conversions, approximately 9%–11%. At 300 °C, the $CO_2$ conversion reached its peak, with *x*Rb/CuZnFe attaining the highest value of ~17%–19%. These results suggest that Rb incorporation improves $CO_2$ activation and hydrogenation, likely due to electronic modifications and improved catalyst stability. At 200 °C, the STY of $C_{2+}$ alcohols, including ethanol, was negligible for all catalysts investigated. Upon increasing the reaction temperature to 250 °C, a significant rise in STY was observed for the Rb-modified catalysts, particularly for 2%Rb/CuZnFe, which reached ~0.5 mmol $g^{-1}$ $h^{-1}$. Further increasing the temperature to 300 °C led to a substantial enhancement in the STY of $C_{2+}$ alcohols, with 8%Rb/CuZnFe exhibiting the highest value (~4.2 mmol $g^{-1}$ $h^{-1}$), followed by 2%Rb/CuZnFe (~3.7 mmol $g^{-1}$ $h^{-1}$).

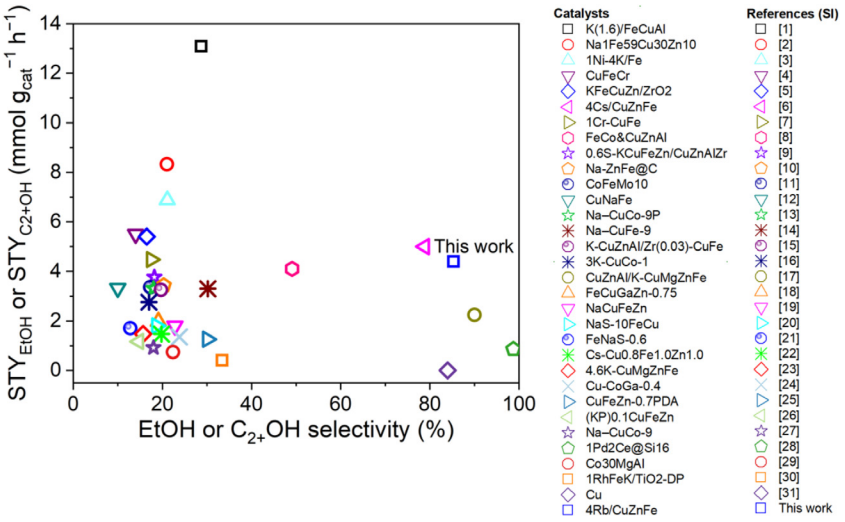


**Fig. 1.** Comparison of literature-reported data with the most active catalyst from this study (4Rb/CuZnFe), illustrating the relationship between STY and selectivity of ethanol or $C_{2+}$OH alcohols, with and/or without CO inclusion. The corresponding reference list is provided in the Supporting Information.

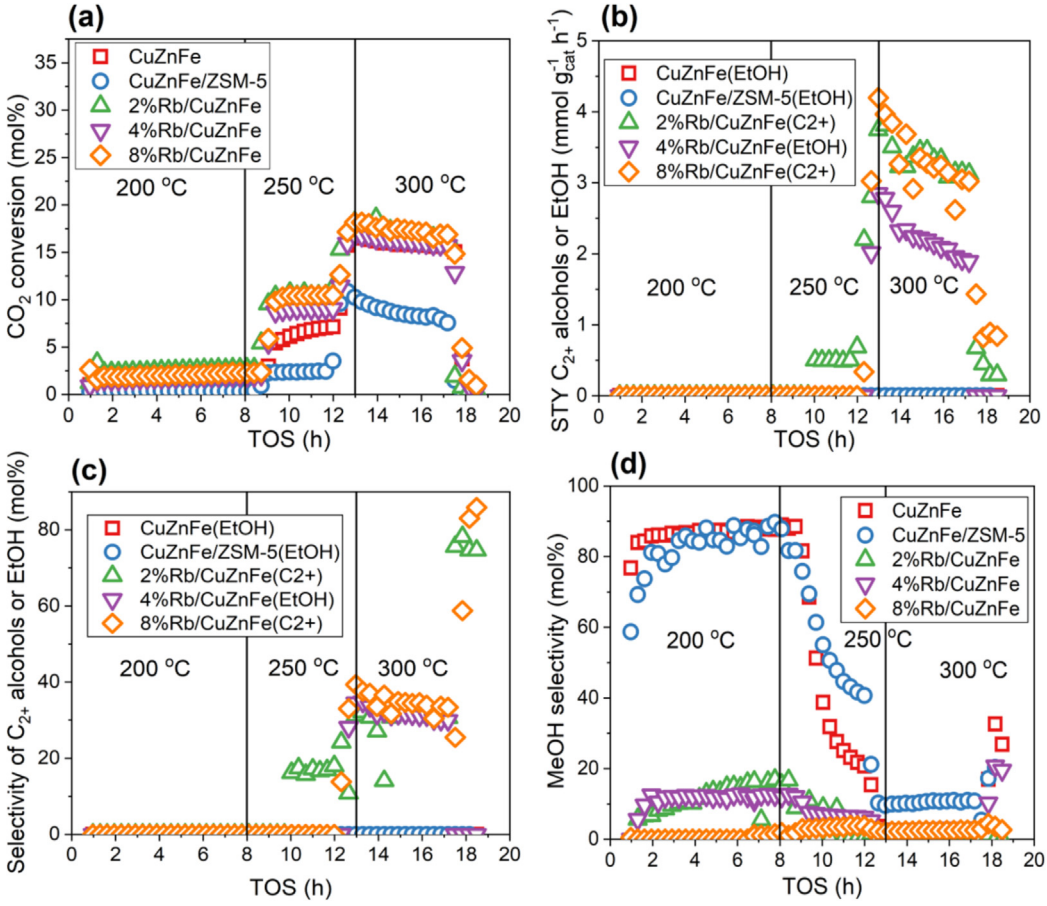


**Fig. 2.** (a) $CO_2$ conversion, (b) STY, (c) selectivity of $C_{2+}$ alcohols and/or EtOH, and (d) MeOH selectivity over CuZnFe and *x*Rb/CuZnFe catalysts in the gas phase. Reaction conditions: $m_{cat}$ = 250 mg; $H_2/CO_2$ = 3; *P* = 20 bar; GHSV = 9917 $h^{-1}$; TOS = 19 h; *T* = 200–300 °C.

The 4%Rb/CuZnFe catalyst demonstrated the highest STY toward ethanol as the primary product, achieving 2.8 mmol $g^{-1}$ $h^{-1}$, while the overall maximum STY reached 4.4 mmol $g^{-1}$ $h^{-1}$ (see below). In contrast, no formation of $C_{2+}$ alcohols was observed over the CuZnFe and CuZnFe/ZSM-5 catalysts, suggesting that the unpromoted CuZnFe catalyst and the zeolite-modified system primarily favoured methanol formation over HA synthesis. The distinction between using EtOH or $C_{2+}$OH in Fig. 2 arises from the experimentally observed product distributions across the catalyst series. For the 4%Rb/CuZnFe catalyst, ethanol was the only $C_{2+}$ alcohol detected in the gas phase under the applied conditions; therefore, both STY and selectivity are reported specifically as EtOH. In

contrast, for catalysts where higher alcohols were also formed in the gas phase, their contribution was included in the total $C_{2+}OH$ STY and selectivity values. Importantly, in the condensed (liquid) phase, $C_{2+}$ alcohols were detected for all catalysts (Fig. 3), enabling a consistent comparison of overall $C_{2+}OH$ selectivity. This approach ensures that the reported values reflect the actual product spectrum of each catalyst rather than imposing uniform metrics that would misrepresent catalysts producing only ethanol.

The STY trends suggest that Rb incorporation plays a crucial role in enhancing $C_{2+}$ alcohol production by promoting C–C coupling over Cu-based catalysts. The selectivity trends in Fig. 2(c) reveal that at 200 °C, all catalysts predominantly formed MeOH, without formation towards HA. As the temperature increased to 250 °C, the selectivity towards $C_{2+}$ alcohols was improved for Rb-modified catalysts, particularly for 2%Rb/CuZnFe (~18%). At 300 °C, the highest selectivity toward $C_{2+}$ alcohols was achieved with the 8%Rb/CuZnFe catalyst, reaching ~86%, followed by 2%Rb/CuZnFe (~78%). In contrast, the 4%Rb/CuZnFe catalyst exhibited the highest selectivity toward ethanol (35%), whereas no formation of higher alcohols was observed over the CuZnFe and CuZnFe/ZSM-5 catalysts. The methanol selectivity trends (Fig. 2d) illustrate the differences among the CuZnFe, CuZnFe/ZSM-5, and Rb-modified CuZnFe catalysts. At 200 °C, the CuZnFe and CuZnFe/ZSM-5 catalysts exhibited similar MeOH selectivity, reaching a maximum of ~88%.

In contrast, the Rb-modified catalysts demonstrated significantly lower MeOH selectivity (12%–16%), with no detectable amounts observed for the 8%Rb/CuZnFe catalyst, indicating a shift toward HA formation. As the reaction temperature increased to 250 °C, MeOH selectivity further declined for the Rb-modified catalysts (3%–7%). At 300 °C, methanol selectivity reached its lowest values, with ~2% observed for the 8%Rb/CuZnFe catalyst and no detectable MeOH for the 2%Rb/CuZnFe catalyst, confirming that Rb promotion effectively redirects selectivity from MeOH toward HA synthesis. Fig. S2 illustrates the CO selectivity over CuZnFe and *x*Rb/CuZnFe catalysts under varying reaction temperatures and TOS. The results indicate that the unmodified CuZnFe catalyst exhibits the lowest CO selectivity, remaining around 20%–30% throughout the experiment, with a slight decrease as the reaction temperature increases.

The introduction of ZSM-5 into the CuZnFe system leads to an increase in CO selectivity to approximately 40%–60%, although selectivity fluctuates, particularly at higher temperatures. The incorporation of Rb into the CuZnFe catalyst significantly enhances CO selectivity, with higher Rb loadings leading to more pronounced effects. At 200 °C, the CO selectivity of Rb-modified catalysts is already notably higher than that of the unmodified CuZnFe system. As the temperature increases to 250 and 300 °C, CO selectivity continues to rise, particularly for catalysts containing 4% Rb and 8% Rb, which maintain selectivity levels above 80%–90% at higher temperatures. Thus, the incorporation of Rb into CuZnFe catalysts had a profound impact on $CO_2$ hydrogenation performance, resulting in enhanced $CO_2$ conversion, increased STY of

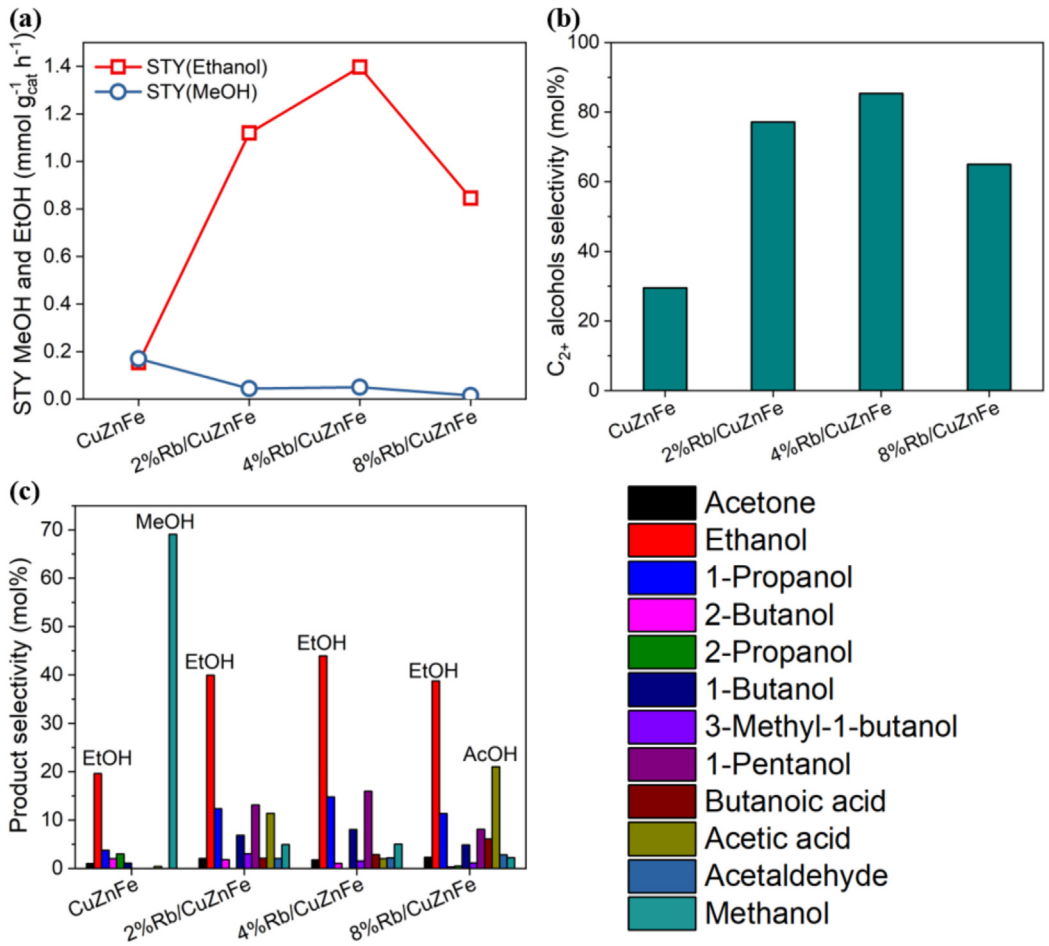


**Fig. 3.** (a) STY and (b, c) product selectivity of condensable products (liquid phase) collected after gas-phase $CO_2$ hydrogenation over CuZnFe and *x*Rb/CuZnFe catalysts after 19 h time-on-stream, using the same temperature program starting at 200 °C and ending at 300 °C. Reaction conditions: $m_{cat}$ = 250 mg; $H_2/CO_2$ = 3; *P* = 20 bar; GHSV = 9917 $h^{-1}$.

$C_{2+}$ alcohols, and improved selectivity toward EtOH and other HA products. At 300 °C, the 8%Rb/CuZnFe catalyst exhibited the highest $CO_2$ conversion, STY, and selectivity toward $C_{2+}$ alcohols, while the highest STY and selectivity for EtOH were achieved with the 4% Rb/CuZnFe catalyst. In contrast, the CuZnFe and CuZnFe/ZSM-5 catalysts remained highly selective for MeOH. These findings indicate that Rb promotion facilitates C–C coupling, thereby suppressing MeOH formation and promoting the synthesis of HA.

The incorporation of alkali metals often leads to complex, nonlinear changes in catalyst behaviour due to simultaneous and competing influences on the electronic properties, dispersion of active phases, and surface acid-base characteristics [33]. The selectivity does not follow a strictly monotonic trend with increasing Rb loading, likely due to the ability of different Rb concentrations to stabilize distinct surface intermediates or promote competing reaction pathways. Characterization data (Brunauer-Emmett-Teller (BET), X-ray photoelectron spectroscopy (XPS), and DRIFTS) indicate that the 4%Rb/CuZnFe catalyst provides a favourable balance of surface oxygen vacancies, preserved crystallinity, and high Cu dispersion. This optimal combination promotes EtOH formation over deeper chain growth or methanation. At 2% or 8% Rb, either insufficient electronic modulation (at low Rb) or excessive surface restructuring/blocking (at high Rb) may shift the pathway toward more $C_{2+}$ alcohols or reduce selectivity altogether. As confirmed by inductively coupled plasma optical emission spectroscopy (ICP-OES) and scanning electron microscopy-energy dispersive X-ray spectroscopy (SEM-EDX) analyses (see below), the actual surface concentrations of Rb do not necessarily correlate with the nominal loadings, likely due to surface enrichment or leaching phenomena occurring during the synthesis process. Thus, the catalytic behaviour reflects the effective surface composition rather than the bulk content, which can also help explain the apparent anomaly of the 4% Rb sample being more ethanol-selective than its neighbours.

### 3.1.2. The effect of Rb loading on the composition of the liquid product and STY

The catalytic performance of CuZnFe and Rb-promoted CuZnFe catalysts was evaluated for the selective production of EtOH and MeOH via gas-phase $CO_2$ hydrogenation, with the resulting condensable liquid products (oxygenates) analysed, as shown in Fig. 3. The STY of both products demonstrated a clear dependence on the Rb loading. The unmodified CuZnFe catalyst showed minimal activity for both EtOH and MeOH formation, with STY values around 0.15 mmol $g_{cat}^{-1}$ $h^{-1}$. This low activity highlights the necessity of promoter modification to enhance the catalytic performance. Notably, no liquid products were detected for the CuZnFe/ZSM-5 catalyst, indicating its limited activity toward the formation of condensable oxygenates under the investigated conditions.

Upon introducing Rb as a promoter, a significant enhancement in EtOH production was observed, with the 4%Rb/CuZnFe catalyst achieving the highest ethanol STY of approximately 1.4 mmol $g_{cat}^{-1}$–$h^{-1}$. This remarkable improvement can be attributed to the synergistic effects of Rb on the active sites, which likely improved $CO_2$ activation and the subsequent C–C coupling steps necessary for ethanol formation. In contrast, the methanol STY exhibited a marginal decrease across the series, with a maximum value of approximately 0.17 mmol $g_{cat}^{-1}$ $h^{-1}$ on the CuZnFe catalyst. This indicates that the presence of Rb favours EtOH production over MeOH, shifting the product distribution. Interestingly, further increasing the Rb loading to 8% resulted in a decrease in the STY of EtOH, suggesting that excessive Rb may block active sites or alter the properties of the catalyst surface detrimentally, reducing its overall efficiency. This trend underscores the importance of optimizing promoter concentration to achieve the desired selectivity and activity. The selective enhancement of EtOH over MeOH with Rb promotion can be attributed to the modification of the electronic and geometric properties of the catalyst surface. Rb likely influences the adsorption strength of $CO_2$-derived intermediates and stabilizes $C_2$ intermediates, promoting EtOH formation. Additionally, the role of Rb in suppressing MeOH formation pathways may contribute to the observed selectivity shift. These findings highlight the critical role of promoter optimization in tailoring the catalytic performance of CuZnFe-based systems for $CO_2$ hydrogenation.

The product selectivity results for $CO_2$ hydrogenation over CuZnFe and Rb-modified CuZnFe catalysts provide valuable insights into the influence of Rb on the reaction pathways and product distribution (Fig. 3b, c). The selectivity trends reveal the diverse range of oxygenates formed, including methanol, ethanol, 1-propanol, 2-butanol, 2-propanol, 1-butanol, 3-methyl-1-butanol, 1-pentanol, butanoic acid, acetic acid, and acetaldehyde. The unmodified CuZnFe catalyst exhibited a high selectivity toward MeOH (~70%), with EtOH selectivity remaining below 20%. This indicates that, without Rb promotion, the primary pathway favoured single-carbon products, reflecting the poor ability of CuZnFe to catalyze C–C coupling reactions. The introduction of Rb dramatically altered the product distribution. For the 2%Rb/CuZnFe catalyst, the methanol selectivity decreased sharply to below 5%, accompanied by a significant increase in EtOH selectivity to ~40%. This shift suggests that Rb facilitates C–C coupling reactions and stabilizes intermediates conducive to EtOH formation. Additionally, a modest increase in selectivity toward HA, such as propanol, butanol, and pentanol, was observed, indicating the improved ability of the catalyst to promote chain growth.

Notably, the 4 wt%Rb/CuZnFe catalyst demonstrates high liquid-phase selectivity to EtOH (~44%) and $C_{2+}$ alcohols (85.3%), with MeOH remaining below 5% (Fig. 3b, c), confirming the preferential formation of higher alcohols. The production of propanol, butanol, and especially pentanol increased, indicating an enhanced capacity for C–C coupling. However, increasing the Rb loading to 8% resulted in a decrease in EtOH selectivity (~38%) and $C_{2+}$ alcohols (~65%), accompanied by a significant rise in acetic acid production. This indicates that excessive Rb promotes secondary oxidation and suppresses ethanol productivity, emphasising that optimal promoter loading is essential for maximising ethanol selectivity. The optimal Rb loading of 4% achieves the highest EtOH selectivity with minimal MeOH formation, while excessive Rb loading promotes side reactions, highlighting the importance of fine-tuning promoter concentration for desired catalytic performance. It should be emphasized that the selectivity of 85.3% to $C_{2+}$OH refers exclusively to the condensed liquid fraction collected in the cold trap at the end of the experiment (Fig. 3b, c). This condensed fraction accounts for only a minor share of the total products and consists of alcohols (methanol, ethanol, and higher alcohols), acids, and aldehydes, while hydrocarbons are not present in the liquid phase. In contrast, the gas phase constitutes the main product stream during continuous operation and was monitored online by micro-GC (gas chromatograph). In the gas phase, ethanol is the only detectable $C_2$ oxygenate, showing a stable selectivity of 44.3%–48.8% over 16 h TOS (see below), while hydrocarbons ($CH_4$, $C_2H_4$, and $C_2H_6$) are observed exclusively in the gas phase. Therefore, the gas-phase and liquid-phase selectivities correspond to different product pools and can not be directly compared. The high $C_{2+}$OH value reflects the enrichment of alcohols in the condensed fraction, whereas the gas phase predominantly contains ethanol with smaller amounts of hydrocarbons.

### 3.1.3. The product distribution over a 4%Rb/CuZnFe catalyst at different reaction temperatures in the gas phase

The results presented in Fig. 4 illustrate the profound impact of reaction temperature on the product selectivity and STY of various

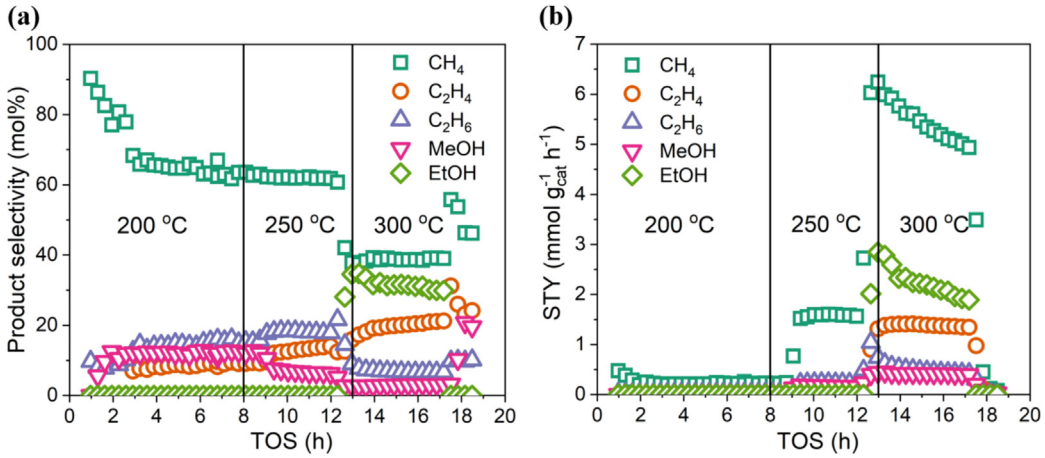


**Fig. 4.** (a) Product selectivity and (b) STY over the 4%Rb/CuZnFe catalyst in the gas phase. Reaction conditions: $m_{cat}$ = 250 mg; $H_2/CO_2$ = 3; $P$ = 20 bar; GHSV = 9917 $h^{-1}$; TOS = 19 h; $T$ = 200–300 °C.

products over the most active 4%Rb/CuZnFe catalyst in the gas phase under 20 bar. The observed trends provide key insights into the catalytic performance and reaction pathways involved in $CO_2$ hydrogenation. At 200 °C, $CH_4$ formation dominates the product distribution, with an initial selectivity exceeding 90%, which gradually stabilizes around 65% after prolonged TOS (Fig. 4a). The high $CH_4$ selectivity at this temperature suggests that methanation pathways are highly favoured under these conditions, likely due to the low activation energy required for $CO_2$ conversion to $CH_4$. The presence of minor quantities of higher hydrocarbons such as ethylene (~8%) and ethane (~16%) indicates limited C–C coupling at this temperature.

Additionally, MeOH (~12%) and EtOH (~1%) appear in trace amounts, suggesting that oxygenate formation is not significantly promoted at low reaction temperatures. The relatively low STY of all products at this stage further supports the limited catalytic activity and selectivity for EtOH synthesis. A significant shift in selectivity is observed when the temperature is increased to 250 °C. $CH_4$ selectivity declines, while the formation of ethylene (~12%) and ethane (~20%) increases, implying an enhancement in C–C bond formation and the suppression of complete hydrogenation pathways. The decreasing of MeOH and the same low amount of EtOH suggest a shift in reaction selectivity away from MeOH production but without a substantial improvement in EtOH formation. These changes can be attributed to an increase in the rate of C–C coupling reactions, which facilitate hydrocarbon growth, while EtOH formation remains kinetically limited under these conditions. Additionally, the enhanced catalytic activity may promote competing pathways, reducing MeOH formation while redirecting intermediates toward hydrocarbon products.

At 300 °C, further modifications in product selectivity are evident. $CH_4$ selectivity decreases below 40%, while EtOH selectivity reaches approximately 35%, with an STY of 2.8 mmol $g_{cat}^{-1}$ $h^{-1}$, marking a substantial enhancement in EtOH production (Fig. 4b). Additionally, ethylene selectivity increases to 21%, with an STY of ~1.4 mmol $g_{cat}^{-1}$ $h^{-1}$, indicating a pronounced shift toward hydrocarbon formation. Interestingly, ethane selectivity decreases to ~8%, suggesting that higher temperatures favour dehydrogenation pathways, leading to olefins rather than full hydrogenation to alkanes. The increase in STY for all products at 300 °C confirms that higher reaction temperatures enhance overall catalytic activity. However, fluctuations in product selectivity at extended TOS indicate potential stability issues, which may arise due to catalyst deactivation caused by sintering, coking, or changes in the structure of active sites. Overall, 4%Rb/CuZnFe favours methane formation at 200 °C, while higher temperatures promote ethanol and ethylene production. Thus, reaction temperature controls the balance between methanation and C–C coupling pathways, enabling optimization of ethanol yield.

The catalytic performance of the 4%Rb/CuZnFe catalyst for $CO_2$ hydrogenation was evaluated based on both gas-phase and condensable (liquid phase) product distributions obtained under gas-phase reaction conditions. The selectivity and STY of EtOH and MeOH were analyzed as a function of TOS over 16 h. The overall organic product spectrum of $CO_2$ hydrogenation can be described by combining gas-phase and condensed products (Fig. S3). For 4% Rb/CuZnFe at 300 °C, the condensed liquid volume after 16 h was only ~1.0 mL, with an ethanol concentration of ~0.50 mol $L^{-1}$ (~0.00050 mol), whereas integration of the gas-phase STY profile indicates ~0.0124–0.0176 mol of ethanol formed in the gas stream. Therefore, ~96%–97% of ethanol remains in the gas phase, while ~3%–4% condenses. Higher alcohols ($C_3$–$C_5$) are preferentially enriched in the liquid phase due to lower volatility, whereas hydrocarbons ($CH_4$, $C_2H_4$, and $C_2H_6$) are detected only in the gas phase. This unified distribution confirms that the gas phase accounts for the majority of carbon-containing products while the condensed fraction reflects heavier oxygenates formed via C–C coupling. The carbon balance is within 90%–98% (Fig. S4), confirming the internal consistency and reliability of the reported data.

The gas-phase catalytic results (Fig. 5a) indicate a stable $CO_2$ conversion of approximately 12% over the 16 h of reaction period. Ethanol selectivity remained relatively high (~45%), while CO selectivity was also significant (~40%–50%), suggesting that the reverse water-gas shift (RWGS) reaction is a major competing pathway. Methanol selectivity was consistently low (<2%), indicating that under these conditions, the catalyst favours $C_2$ oxygenates over $C_1$ products. The STY profiles in Fig. 5(b) further support these findings, showing a high initial STY of EtOH (~4.4 mmol $g_{cat}^{-1}$ $h^{-1}$), which gradually declines but remains stable around ~ 3.0 mmol $g_{cat}^{-1}$ $h^{-1}$ during 16 h. In contrast, the STY of MeOH is negligible (<0.3 mmol $g_{cat}^{-1}$ $h^{-1}$) throughout the reaction duration, reinforcing the preferential selectivity of the catalyst toward EtOH.

In the condensable (liquid phase) product fraction (Fig. 5c), EtOH was the dominant product across different reaction conditions, reaching the highest selectivity (~30%–44%), followed by HA, including 1-propanol (~9%–14%), 1-butanol (~4%–7%), and 1-pentanol (~7%–16%). These results suggest that the catalyst facili-

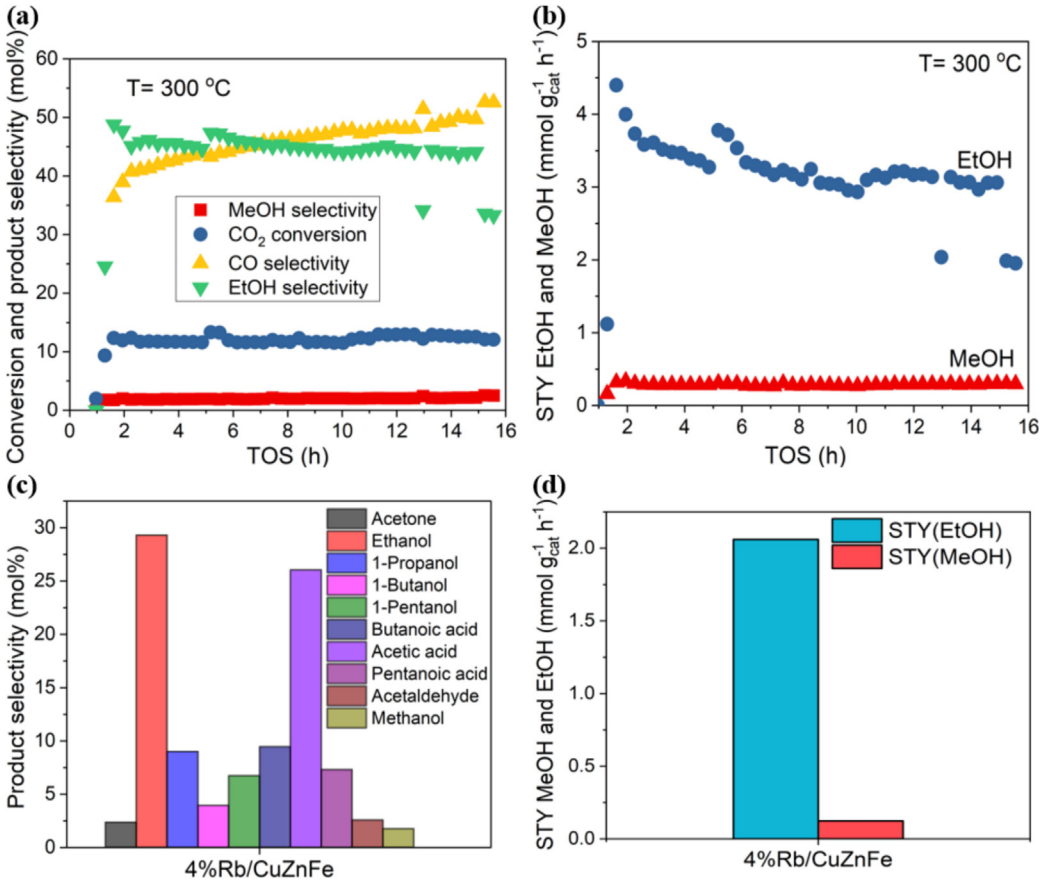


**Fig. 5.** (a, b) Gas-phase product selectivity and STY and (c, d) condensable product (liquid phase) selectivity and STY over the 4%Rb/CuZnFe catalyst during gas-phase $CO_2$ hydrogenation after 16 h time-on-stream. Reaction conditions: $m_{cat}$ = 250 mg; $H_2/CO_2$ = 3; $P$ = 20 bar; GHSV = 9917 $h^{-1}$; $T$ = 300 °C.

tates C–C coupling, leading to the formation of higher oxygenates. The presence of acetic acid, butanoic acid, and pentanoic acid in the condensable (liquid phase) products indicates possible secondary oxidation or condensation reactions during $CO_2$ hydrogenation. The increased acetic acid selectivity observed in Fig. 5(c) is likely attributed to the immediate exposure of the fresh catalyst to a higher initial temperature, which may influence the formation and evolution of surface intermediates, favour alternative oxidation pathways, and induce distinct deactivation mechanisms compared to the gradual temperature ramp shown in Fig. 3(c). Such differences in thermal treatment and TOS can modify the distribution and oxidation state of active sites, ultimately altering the product selectivity. The relatively low MeOH selectivity (<2%) aligns with the gas-phase results, further confirming the catalyst preference for EtOH and HA over MeOH.

The STY values in Fig. 5(d) show that EtOH has a much higher STY compared to MeOH in the condensable (liquid phase) products, further emphasizing the selectivity of the 4%Rb/CuZnFe catalyst toward EtOH production. This could be attributed to the electronic and structural properties of the Rb-modified CuZnFe catalyst, which may enhance the stabilization of key $C_2$ intermediates, while suppressing excessive hydrogenation to MeOH. The detection of HA in the condensable (liquid phase) products indicates that subsequent chain growth via CO insertion or aldol-type condensation mechanisms is also taking place. Additionally, the presence of acids suggests that some intermediates may undergo oxidation under reaction conditions. This could be a competing pathway, where acetaldehyde, ethanol, or HA is partially oxidized to acetic acid or other carboxylic acids, depending on the basicity and redox properties of the catalyst.

### 3.2. Catalyst characterizations

Fig. 6(a) shows the $N_2$ adsorption-desorption isotherms of the CuZnFe and *x*Rb/CuZnFe catalysts. All samples display type IV isotherms with hysteresis loops classified as type $H_3$, which are characteristics of mesoporous materials [18]. Among the catalysts, the 2%Rb/CuZnFe sample exhibits the highest $N_2$ adsorption volume, indicating a significant increase in surface area and porosity compared to the undoped CuZnFe catalyst. The increase in adsorption for the 2%Rb/CuZnFe catalyst suggests that the introduction of Rb at this level effectively enhances the surface area, porosity, or mesostructured formation, providing more accessible active sites for catalysis. The 8%Rb/CuZnFe catalyst also shows an increase in adsorption, though it is lower than that of the 2%Rb/CuZnFe sample, possibly due to pore blocking or collapse of the mesoporous structure. In contrast, the 4%Rb/CuZnFe catalyst displays a decrease in $N_2$ adsorption compared to CuZnFe, despite being the most catalytically active. The BJH pore size distribution curves (Fig. 6b) provide further insight into the textural characteristics of the catalysts. The pore size calculated using the BJH equation from the desorption branch shows that the 2%Rb/CuZnFe and 8%Rb/CuZnFe catalysts have a narrower pore size distribution, ranging from 20 to 100 nm, with peaks at 61 and 59 Å, respectively.

In contrast, the CuZnFe and 4%Rb/CuZnFe catalysts display broader pore size distributions, extending from 20 to 1000 nm, indicating the presence of a wider range of pore sizes. The CuZnFe catalyst has a peak pore diameter (PD) of approximately 35 Å, indicating a broad distribution of pore sizes that contributes to its overall porosity. The 4%Rb/CuZnFe catalyst exhibits a similar peak PD around 35 Å. However, despite having a comparable broad pore

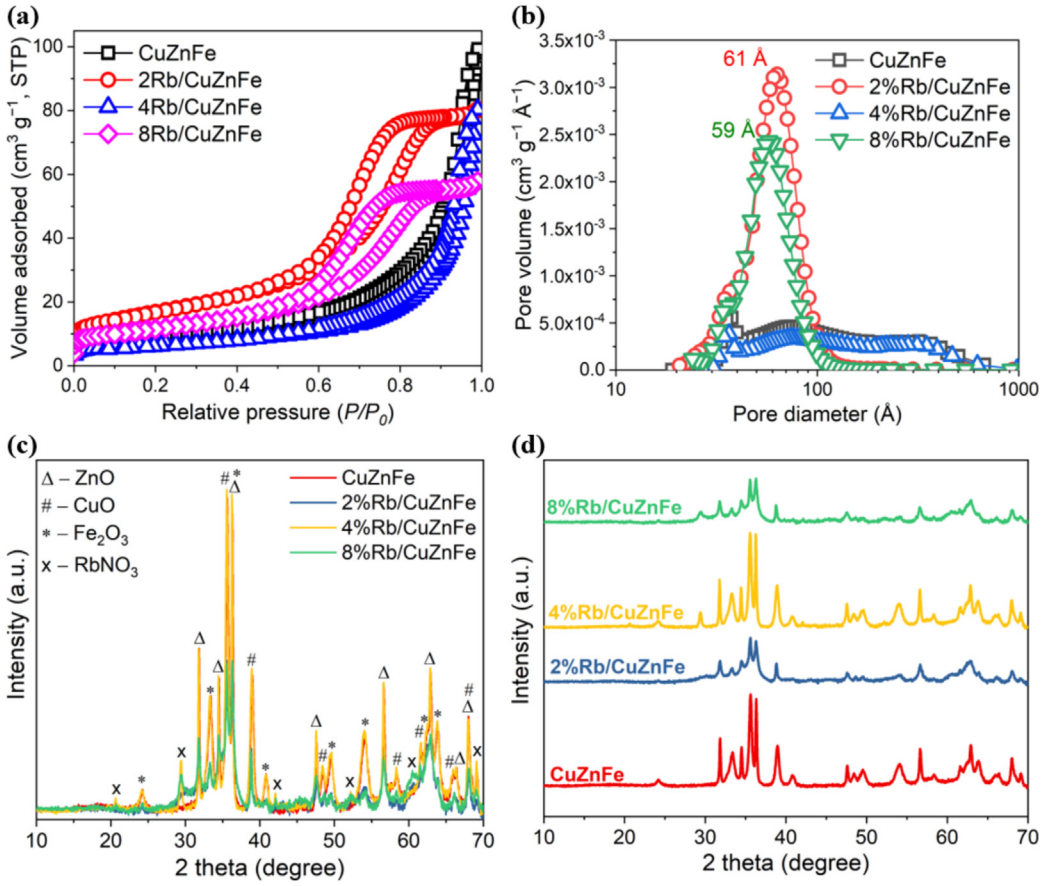


**Fig. 6.** (a) $N_2$ adsorption-desorption isotherms, (b) BJH pore size distribution, and (c, d) XRD patterns of the CuZnFe and *x*Rb/CuZnFe catalysts.

size distribution, the 4%Rb/CuZnFe catalyst demonstrates significantly superior catalytic performance. Although the 4%Rb/CuZnFe catalyst has a slightly lower surface area than the unmodified sample, its pore architecture remains sufficient to ensure mass transport and accessibility to the Cu-Fe and Cu-Zn active interfaces. The enhanced activity is therefore attributed primarily to electronic promotion and oxygen vacancy formation rather than textural properties.

The elemental compositions of the catalyst samples, including the Cu, Zn, Fe, and Rb contents, were analysed using ICP-OES (Table 1). An interesting trend in Cu content across the Rb-modified CuZnFe catalysts was revealed. While increasing Rb loading generally correlates with a reduction in Cu content, likely due to leaching, an exception was observed in the 4%Rb/CuZnFe sample, which maintained a high Cu content of 18 wt%. This result suggests that an optimal Rb loading of around 4 wt% might enhance the stability of Cu within the catalyst matrix. The relatively high Cu content in the 4%Rb/CuZnFe sample could be attributed to a stabilizing effect provided by the moderate addition of Rb. At this specific loading, Rb may occupy positions within the catalyst structure that support Cu adherence to the matrix, potentially reducing the tendency for Cu leaching seen at both lower and higher Rb concentrations. This stabilizing interaction could be due to Rb ions at 4 wt% facilitating a favourable electrostatic environment or anchoring effect that retains Cu within the matrix, thereby minimizing its dissolution or detachment during synthesis or reaction.

**Table 1**
Elemental composition and structural properties of the CuZnFe and *x*Rb/CuZnFe catalysts.

| Catalyst | Rb[a] (wt%) | Cu[a] (wt%) | Zn[a] (wt%) | Fe[a] (wt%) | $S_{BET}$[b] ($m^2\ g^{-1}$) | $S_{micro}$[b] ($m^2\ g^{-1}$) | $S_{meso}$[b] ($m^2\ g^{-1}$) | $V_{micro}$[c] ($cm^3\ g^{-1}$) | $V_{total}$[c] ($cm^3\ g^{-1}$) | $V_{meso}$[c] ($cm^3\ g^{-1}$) | PD[d] (nm) | Crystallite size[e] (nm) | RC[e] (%) | RC vs. CuZnFe[e] (%) |
|---|---|---|---|---|---|---|---|---|---|---|---|---|---|---|
| CuZnFe | – | 19.0 | 21.0 | 41.0 | 31.7 | 1.9 | 29.8 | $7.6\times10^{-4}$ | 0.149 | 0.148 | 15.5 | 20.6 | 96.5 | 96.5 |
| 2%Rb/CuZnFe | 2.0 | 13.0 | 21.0 | 43.0 | 60.0 | 3.8 | 56.2 | $1.6\times10^{-3}$ | 0.123 | 0.121 | 6.1 | 18.4 | 79.5 | 60.2 |
| 4%Rb/CuZnFe | 3.0 | 18.0 | 19.0 | 38.0 | 23.0 | 4.3 | 18.7 | $2.1\times10^{-3}$ | 0.119 | 0.197 | 16.6 | 21.3 | 95.9 | 99.6 |
| 8%Rb/CuZnFe | 6.0 | 12.0 | 20.0 | 39.0 | 41.2 | 4.7 | 36.5 | $2.2\times10^{-3}$ | 0.088 | 0.086 | 5.9 | 19.8 | 76.1 | 54.5 |

[a] ICP-OES.
[b] BET method.
[c] t-plot method.
[d] Average pore diameter measured from the desorption branch according to the BJH method.
[e] The crystallite size and relative crystallinity (RC) were obtained from XRD data.

In contrast, lower Rb loadings may not provide sufficient stabilization, while higher Rb loadings might promote competitive ion exchange or destabilize Cu adherence to the support. These observations underscore the importance of optimizing Rb content in the CuZnFe catalyst to balance Cu stability and prevent leaching during the impregnation/calcination steps, ultimately enhancing the catalytic performance in $CO_2$ hydrogenation reactions.

Table 1 shows that the specific BET surface area ($S_{BET}$) of CuZnFe increases significantly with the introduction of Rb, with the 2%Rb/CuZnFe sample showing the highest value at 60.0 $m^2$ $g^{-1}$. This is almost double that of the parent CuZnFe catalyst (31.7 $m^2$ $g^{-1}$), suggesting that Rb addition enhances the surface area. However, further increases in Rb content lead to a decrease in surface area, with 4%Rb/CuZnFe exhibiting the lowest $S_{BET}$ at 23.0 $m^2$ $g^{-1}$. This could be due to excessive Rb loading, potentially causing partial blockage of pores or pore collapse [18]. When the Rb loading was increased to 8%, the $S_{BET}$ rose to 41.2 $m^2$ $g^{-1}$. This increase suggests that while excessive Rb can lead to pore blockage at intermediate levels (as observed with the 4%Rb/CuZnFe catalyst), higher Rb concentrations might induce structural reorganization or the formation of new mesopores. This effect could be related to changes in crystalline phases or the redistribution of Rb at higher loadings, which can enhance surface exposure and improve the overall porosity of the catalyst. While the increase in $S_{BET}$ at 2 wt% alkali metal loading appears significant, the consistent observation of this trend across various alkali-modified samples (not limited to Rb) suggests a systematic effect. However, we acknowledge that the underlying mechanism may involve subtle changes in crystallization dynamics, metal dispersion, or particle agglomeration during synthesis. Therefore, we refrain from over-interpreting this trend and do not attribute it solely to a "textural promotion" effect by the alkali metal.

The mesoporous surface area ($S_{meso}$) follows a similar trend, with the 2%Rb/CuZnFe catalyst showing the highest mesoporous surface area (56.2 $m^2$ $g^{-1}$). This value sharply drops with higher Rb content, indicating that higher Rb doping might alter the mesoporous structure, reducing its overall effectiveness for certain catalytic processes. The microporous surface area ($S_{micro}$), although relatively small, shows a gradual increase with increasing Rb content, which suggests some degree of pore structure modification. The total pore volume ($V_{total}$) and mesoporous volume ($V_{meso}$) show an interesting pattern. Despite the increase in surface area for the 2%Rb/CuZnFe sample, its total pore volume decreases slightly compared to CuZnFe, from 0.149 to 0.123 $cm^3$ $g^{-1}$. This is likely due to changes in pore structure, as indicated by the shift in PD discussed below. The 4%Rb/CuZnFe catalyst shows a slightly reduced pore volume, while 8%Rb/CuZnFe has the lowest total pore volume (0.088 $cm^3$ $g^{-1}$), possibly due to further structural collapse or compaction caused by the high Rb loading.

The average PD shows substantial variation with Rb addition. The parent CuZnFe catalyst has an average PD of 15.5 nm, but this drastically decreases to 6.1 nm for the 2%Rb/CuZnFe catalyst and to 5.9 nm for the 8%Rb/CuZnFe sample. This decrease suggests that Rb doping influences the pore size distribution by narrowing the pores, which is consistent with the BJH pore size distribution data (Fig. 6b). Interestingly, the 4%Rb/CuZnFe sample shows a larger PD of 16.6 nm, which deviates from the general trend. This could indicate that at moderate Rb doping levels, there is a restructuring or reorganization of the pore system, possibly due to Rb acting as a template for larger mesopores.

The X-ray diffraction (XRD) patterns displayed in Fig. 6(c, d) exhibit the profiles of the CuZnFe and *x*Rb/CuZnFe catalysts. The primary crystalline constituents for the catalysts prior to the reaction encompass ZnO (COD No. 96-900-4182) with peaks at 2$\theta$ angles of 31.8°, 34.5°, 36.3°, 47.6°, 56.7°, 62.9°, 66.4°, and 68.0°, CuO (COD No. 96-901-6327) with peaks at 2$\theta$ angles of 35.6°, 38.9°, 48.4°, 58.4°, 61.7°, 66.4°, and 68.0°, $Fe_2O_3$ (COD No. 96-154-6384) with peaks at 2$\theta$ angles of 24.2°, 33.3°, 35.6°, 40.9°, 49.6°, 54.1°, 62.5°, and 63.9°, and $RbNO_3$ (COD No. 96-210-7327) with peaks at 2$\theta$ values of 20.7°, 29.5°, 42.2°, 52.3°, 61.3°, 65.4°, and 69.4°.

The presented data in Table 1 and Fig. 6(c, d) illustrate the effects of varying Rb loadings on the crystallite size and relative crystallinity (RC) of CuZnFe-based catalysts. The results highlight significant structural changes as Rb content increases, which have implications for catalyst stability and performance. XRD analysis revealed that all catalysts maintained similar crystallite sizes in the range of 18.4–21.3 nm, with minor variations that fall near the instrumental error margin. However, the 4%Rb/CuZnFe catalyst exhibited a crystallite size of 21.3 nm and a RC of 95.9%, nearly identical to the unmodified CuZnFe catalyst (RC = 96.5%), indicating excellent structural preservation. This near-complete retention of crystallinity suggests that 4% Rb loading achieves an optimal balance between introducing Rb and maintaining structural order. Such stability is likely advantageous for catalytic performance, as it preserves active sites and reduces the risk of deactivation due to structural degradation. In contrast, the 8%Rb/CuZnFe catalyst showed a notable decrease in RC to 76.1%, suggesting partial structural disorder at higher Rb loading. This trend highlights that moderate Rb incorporation maintains crystalline integrity, while excessive Rb may disrupt the structure, weaken the catalyst stability, and reduce its performance in catalytic applications by diminishing the number of accessible active sites and increasing the likelihood of deactivation.

The XRD pattern of the spent 4%Rb/CuZnFe catalyst (Fig. S5) reveals well-defined reflections corresponding to ZnO, metallic Cu, and $Fe_5C_2$, demonstrating the coexistence of these crystalline phases after $CO_2$ hydrogenation. The characteristic ZnO reflections at ~31.8°, 34.4°, 36.3°, 47.5°, 56.6°, 62.8°, 67.9°, and 69.1° suggest that the ZnO structure remains largely preserved under reaction conditions. The presence of metallic Cu peaks at ~43.3°, 50.4°, and 74.1° confirms the formation of reduced copper species, consistent with its established role as an active phase for $CO_2$ activation and hydrogenation. Notably, diffraction signals assigned to $Fe_5C_2$ appear at ~39.2°, 41.3°, and 43.3°, providing compelling evidence for iron carburization during reaction. The stabilization of $Fe_5C_2$ is known to enhance C–C coupling pathways, supporting the formation of ethanol and higher alcohols in agreement with catalytic performance trends [34–36].

The simultaneous presence of Cu, ZnO, and $Fe_5C_2$ indicates strong metal-oxide interactions within the trimetallic matrix, promoting the formation of multifunctional active sites capable of balancing $CO_2$ activation, hydrogen spillover, and C–C bond coupling pathways. Previous studies [37,38] have shown that the superior performance of Cu-Fe systems arises from the synergistic interplay between $Fe_5C_2$ and Cu, where Cu facilitates $CO_2/H_2$ activation and hydrogen transfer, while $Fe_5C_2$ provides chain-growth sites for C–C coupling (via $CO^*$ insertion into $CH_3^*$). In the present catalyst, the Fe content enables the formation of highly dispersed $Fe_5C_2$ domains intimately interfaced with Cu, resulting in the development of an efficient Cu-$Fe_5C_2$ active interface. This structural configuration enhances intermediate stabilization and carbon-chain propagation, consistent with the observed high selectivity toward ethanol and $C_{2+}$ alcohols. Additionally, Rb serves as an electronic and structural promoter that facilitates Fe carburization, while the extent and stability of the carbide phase are further tuned by interactions with the surrounding metal-oxide matrix, collectively contributing to the optimized catalytic performance.

The SEM images provide detailed insights into the morphological differences between the CuZnFe catalyst and the 4%Rb/CuZnFe catalyst (Fig. 7), revealing key structural features that underpin the enhanced catalytic performance of the Rb-modified catalyst. The

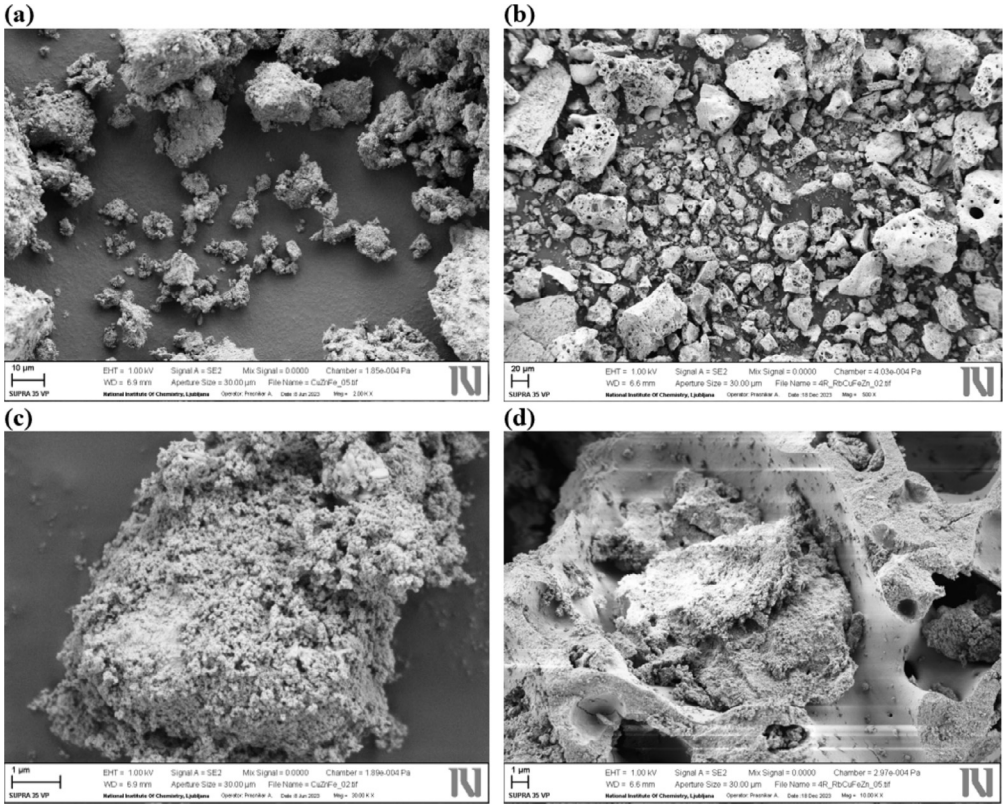


**Fig. 7.** SEM images of (a, c) CuZnFe and (b, d) 4%Rb/CuZnFe samples.

CuZnFe catalyst (Fig. 7a, c) demonstrates a relatively uniform distribution of particles with varying sizes. The particles exhibit aggregation, forming larger clusters with irregular shapes. The surface texture is notably rough, which is generally indicative of relatively high surface area, which is a beneficial characteristic for catalytic activity. However, the extent of aggregation in the CuZnFe sample could limit the accessibility of reactants to active sites, potentially constraining its catalytic efficiency.

In contrast, the 4%Rb/CuZnFe catalyst (Fig. 7b, d) exhibits significant morphological transformations following the incorporation of Rb. The particles display a more open and porous sponge-like structure, with reduced aggregation compared to the CuZnFe catalyst. This increased porosity is particularly advantageous, as it enhances the accessibility of reactants to the active catalytic sites, thereby improving catalytic activity and selectivity. The smoother surface of the 4%Rb/CuZnFe particles compared to the unmodified catalyst may also facilitate more uniform interactions with reactants, which could contribute to the improved catalytic performance observed in this study.

The presence of Rb in the catalyst may facilitate this sintering process, leading to structural modifications that improve the mechanical stability of the catalyst, while minimizing issues like leaching of active components. Despite the potential for sintering to reduce surface area, the enhanced porosity and structural integrity observed in the Rb-modified catalyst suggest that the Rb content has been optimized to balance these effects. The open structure ensures adequate access to active sites, while the increased thermal stability minimizes deactivation over time. The observed morphological changes align closely with the enhanced catalytic performance metrics of the 4%Rb/CuZnFe catalyst.

The elemental composition of the CuZnFe and *x*Rb/CuZnFe catalysts was analyzed using SEM-EDX, as summarized in Table S2. The pristine CuZnFe catalyst exhibits an average Cu content of 20.1 wt%, Fe of 35.6 wt%, Zn of 14.6 wt%, and O of 29.7 wt%. The relatively high Fe content suggests its dominant presence in the catalyst structure, likely contributing to the catalyst redox properties. The Zn fraction remains stable across multiple scans, indicating a homogeneous distribution of Zn within the catalyst matrix. Upon modification with Rb, notable compositional changes occur. The introduction of 2% Rb leads to a decrease in Cu content to 15.3 wt%, accompanied by an increase in Fe (40.6 wt%) and Zn (20.8 wt%). The incorporation of Rb may alter the surface dispersion of active metal sites, thereby influencing metal-support interactions. The oxygen content remains within the expected range (21.0 wt%), suggesting that oxidation state variations upon Rb addition are minimal. At the highest Rb loading (8%), the Cu content drops significantly to 13.4 wt%, while Fe and Zn increase to 38.8 wt% and 19.5 wt%, respectively. The oxygen content also declines to 23.9 wt%, which may be linked to structural modifications induced by Rb incorporation. The higher Rb content (4.4 wt%) suggests more successful deposition compared to lower loading levels. The increased Fe fraction at higher Rb loadings implies that Rb may influence the catalyst surface chemistry, potentially by altering the oxidation states of Fe and Cu.

Interestingly, increasing the Rb loading to 4 wt% results in a notable increase in Cu content to 20.5 wt%, while Fe and Zn remain comparable at 36.9 wt% and 14.6 wt%, respectively. The oxygen content decreases slightly to 26.1 wt%, which may indicate structural modifications due to the presence of Rb. However, the Rb content (1.9 wt%) is lower than the nominal loading, suggesting limitations in Rb incorporation or possible leaching effects during the preparation process. The increase in Cu content for 4%Rb/CuZnFe, compared to all other studied samples, suggests that 4 wt% Rb provides an optimal environment for Cu stabilization. At this concentration, Rb may promote stronger metal-support interactions, reducing Cu mobility and preventing its migration

or sintering during catalyst synthesis. In contrast, at lower Rb loadings (2% Rb), this stabilization effect is less pronounced, leading to lower Cu retention. At higher Rb loadings (8% Rb), excessive Rb may disrupt the catalyst structure or induce phase segregation, thereby reducing Cu incorporation. Additionally, Rb is known to alter the electronic properties of metal oxides, influencing the deposition and stabilization of other metals. At an optimal 4% Rb, the modified surface charge may enhance Cu anchoring, preventing Cu leaching or loss during synthesis. However, at higher Rb loadings (8% Rb), excessive Rb could introduce excessive structural changes, potentially reducing Cu incorporation. Thus, these results suggest that the 4%Rb/CuZnFe catalyst exhibits a unique composition where Cu retention is maximized, likely due to an optimal balance between Rb-induced stabilization and structural integrity.

The structural and compositional characteristics of the CuZnFe and 4%Rb/CuZnFe catalysts were investigated using scanning transmission electron microscopy (STEM)-EDX elemental mapping (Fig. 8) and STEM-BF (bright field) imaging (Fig. S6), revealing significant modifications upon Rb incorporation. The bright-field STEM image of the CuZnFe catalyst (Fig. 8a) shows a highly agglomerated morphology with well-dispersed nanoparticles. EDX elemental mapping confirms the homogeneous distribution of Cu, Zn, Fe, and O across the catalyst, suggesting a well-integrated multi-metallic system. The even dispersion of these elements is essential for ensuring uniform active site distribution and optimal catalytic performance. However, the introduction of Rb into the catalyst matrix (Fig. 8b and Fig. S2b) results in notable morphological and compositional changes. The bright-field STEM image of the 4%Rb/CuZnFe sample reveals larger and more aggregated structures compared to the pristine CuZnFe catalyst, suggesting an influence of Rb on particle growth and sintering behaviour. The EDX elemental mappings confirm the presence of Rb, which appears well-dispersed throughout the sample, indicating successful incorporation into the catalyst structure. The redistribution of elements upon Rb modification may significantly influence catalytic behaviour. The presence of Rb can alter the electronic properties of Cu and Fe species, affecting their reducibility and metal-support interactions.

Further insights into the structural evolution induced by Rb addition are provided by the high-resolution STEM-BF images shown in Fig. S2. The CuZnFe catalyst (Fig. S2a) exhibits a dispersed nanoparticulate structure with no visible signs of sintering or large crystalline domains. The small particle size and relatively high dispersion suggest a high surface area, which is typically beneficial for catalytic performance due to enhanced accessibility of active sites. However, upon modification with Rb, the 4%Rb/CuZnFe catalyst displays more pronounced morphological changes. A distinctive hexagonal particle is observed (Fig. S2b), suggesting the formation of a secondary crystalline phase. This structural transformation may indicate the segregation of certain elements or the emergence of a new phase that alters the physicochemical properties of the catalyst. The increased particle size and the formation of well-defined crystallites suggest that Rb incorporation may induce restructuring effects, potentially modifying the accessibility and stability of active sites. Thus, the observed changes in particle morphology, elemental distribution, and potential phase segregation suggest that Rb serves not only as an electronic promoter but also as a structural modifier. These effects could impact catalytic activity, selectivity, and stability in $CO_2$ hydrogenation reactions.

X-ray photoelectron spectroscopy (XPS) measurements were conducted to investigate the elemental composition and electronic states of the CuZnFe and *x*Rb/CuZnFe catalysts, as presented in Fig. 9. The survey spectra (Fig. 9a) confirm the presence of Cu, Zn, Fe, O, and Rb in the catalysts, with no detectable impurities, indicating the high purity of the synthesized materials. The O 1*s* spectra (Fig. 9b) exhibit a prominent peak centred around 529.6–531.2 eV, which can be attributed to lattice oxygen and surface-adsorbed oxygen species. The primary peak at approximately 529.2–529.6 eV corresponds to metal–oxide bonds (M–O), while the component at the higher binding energy (BE) of ~531.2 eV is typically associated with hydroxyl species and adsorbed oxygen. Notably, the O 1*s* peak shifts slightly with increasing Rb content, suggesting modifications in the electronic environment, possibly due to changes in oxygen vacancies or altered metal-oxygen interactions upon Rb incorporation. The most pronounced shift was observed for the 4%Rb/CuZnFe catalyst, with the main O 1*s* peak appearing at 529.2 eV, along with the most prominent shoulder at 531.2 eV. This catalyst also exhibited the highest activity in $CO_2$ hydrogenation, yielding ethanol and HA, which aligns with the observed electronic modifications. The correlation between electronic structure changes and catalytic performance suggests that Rb plays a crucial role in tuning the active sites and enhancing the reaction pathway for selective alcohol synthesis.

The Zn 2*p* spectra (Fig. 9c) exhibit the Zn $2p_{3/2}$ peak at 1020.8–1021.5 eV, which is characteristic of $Zn^{2+}$ in ZnO. The variation in BE among the samples suggests a possible alteration in the Zn electronic structure upon Rb incorporation. Notably, the Zn 2*p* peak shifts to lower BE in the Rb-modified catalysts, decreasing from 1021.5 to 1020.8 eV, indicating a change in the local electronic environment of Zn. This shift suggests an increased electron density around Zn, potentially due to charge redistribution or modified metal-support interactions induced by Rb addition. While the shift is observed across all Rb-containing samples, it is less pronounced in the 4%Rb/CuZnFe catalyst, implying that at this loading, the electronic effects may be counterbalanced by other structural modifications. The Rb 3*d* region (Fig. 9d) reveals a peak centred around 110.5 eV, confirming the successful incorporation of Rb into the catalyst structure. The consistent peak position across the Rb-containing samples suggests that Rb exists in a similar oxidation state in all compositions, likely as $Rb^+$ species interacting with the CuZnFe surface.

The Cu 2*p* XPS spectra, presented in Fig. S7, reveal the Cu $2p_{3/2}$ and Cu $2p_{1/2}$ core-level peaks centred at approximately 933.3 and 953.5 eV, respectively. These BE values are characteristic of $Cu^{2+}$ species in CuO, confirming that copper in the catalysts predominantly exists in an oxidized state. The absence of a strong satellite peak at higher BE further supports the dominance of $Cu^{2+}$ over metallic $Cu^0$ species. The CuZnFe sample exhibits significantly lower peak intensity compared to the Rb-modified catalysts, indicating a lower surface concentration of Cu species. Upon Rb addition, the Cu 2*p* peak intensities increase, suggesting enhanced Cu surface exposure and potential modifications in the electronic structure. This increase in intensity is particularly noticeable for the 2%Rb/CuZnFe and 8%Rb/CuZnFe samples. However, in the 4% Rb/CuZnFe catalyst, the Cu 2*p* signal remains strong but exhibits a lower intensity compared to the other Rb-containing samples. The BE of Cu $2p_{3/2}$ remains nearly constant across all Rb-modified samples, indicating that Rb incorporation does not significantly alter the oxidation state of Cu but may influence its electronic environment. Notably, a small shift in BE is observed for the 4%Rb/CuZnFe sample, where the Cu $2p_{1/2}$ peak shifts from 953.5 to 952.6 eV. This shift, along with variations in peak intensity and shape, suggests electronic interactions between Cu and Rb species, which could influence catalytic performance. The surface composition of CuZnFe and *x*Rb/CuZnFe catalysts, as determined by XPS analysis, is presented in Tables S3 and S4. Overall, the XPS results provide strong evidence that Rb is effectively incorporated into the CuZnFe catalyst without introducing impurities. The observed shifts in BE, particularly in the O 1*s*, Zn 2*p*, and Cu 2*p* spectra, indicate that Rb influences the electronic properties of the catalyst, which could affect its catalytic performance.

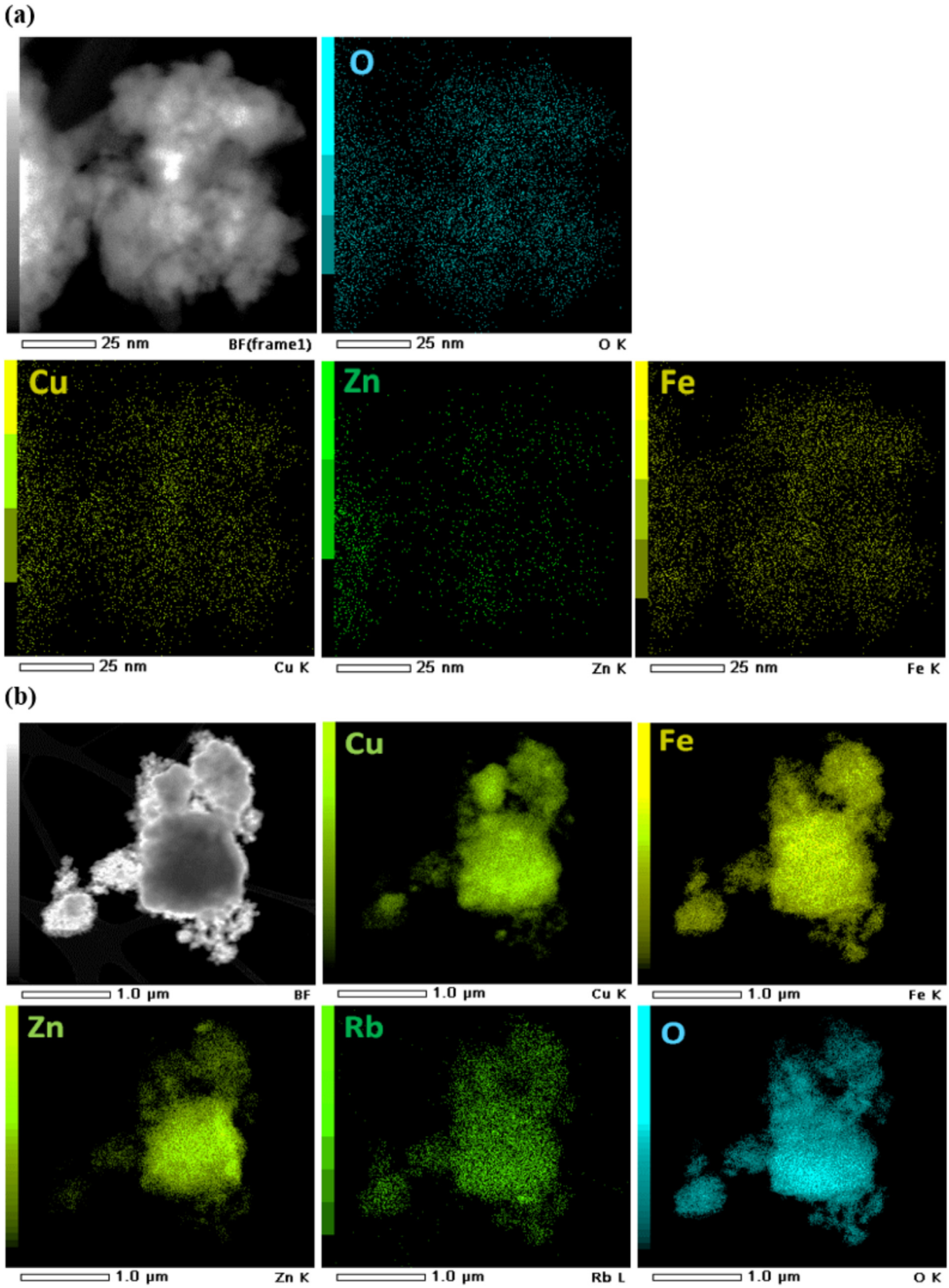


**Fig. 8.** STEM images and EDX elemental mappings of (a) CuZnFe and (b) 4%Rb/CuZnFe samples.

To gain deeper insights into the surface oxygen species and their distribution in CuZnFe and *x*Rb/CuZnFe catalysts, the O 1*s* XPS spectra were deconvoluted, as shown in Fig. 10. The spectra reveal two distinct oxygen species: lattice oxygen ($O_L$) at approxi-

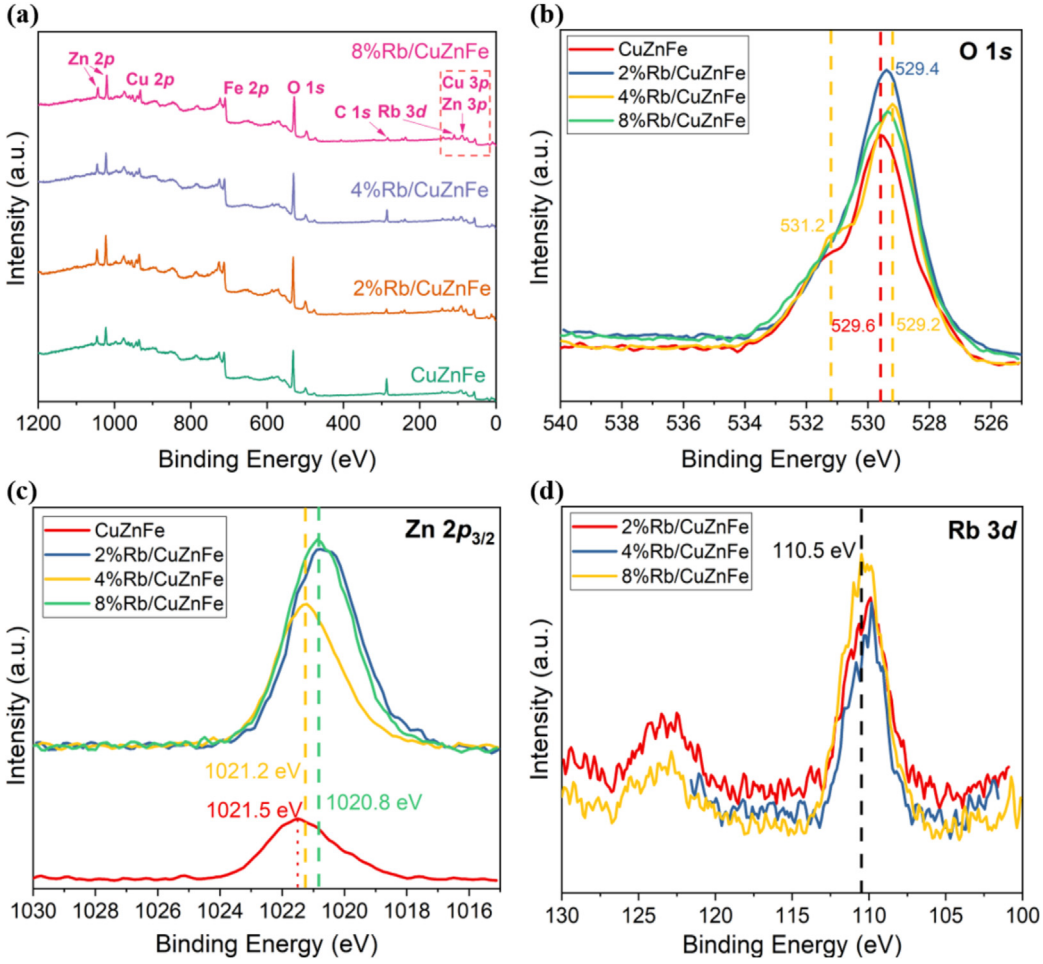


**Fig. 9.** XPS spectra of (a) survey, (b) O 1*s*, (c) Zn 2*p*, and (d) Rb 3*d* in the CuZnFe and *x*Rb/CuZnFe catalysts.

mately 529.0–530.0 eV and oxygen vacancies or adsorbed oxygen species ($O_V$) appearing at higher BE (~531.0–531.5 eV). The relative contributions of these components provide crucial information regarding the influence of Rb on the electronic environment and defect structure of the catalysts. The pristine CuZnFe catalyst (Fig. 10a) exhibits a dominant $O_L$ peak, indicating a well-structured metal-oxide framework with a low concentration of oxygen vacancies.

With the incorporation of Rb (Fig. 10b–d), notable shifts in the $O_L/O_V$ ratio are observed. Specifically, the percentage of $O_V$ increases with Rb doping up to 4%Rb/CuZnFe but decreases slightly for 8%Rb/CuZnFe (Fig. 10e). This suggests that Rb addition initially promotes the formation of oxygen vacancies, which are known to enhance catalytic activity by facilitating oxygen mobility and reactant activation. The maximum $O_V$ concentration (35.2%) is observed for the 4%Rb/CuZnFe sample, whereas a decrease to 25.5% for 8%Rb/CuZnFe suggests partial passivation or structural stabilization at a higher Rb loading. The trend in $O_V$ formation implies that moderate Rb incorporation induces defect sites, which could enhance redox properties and catalytic performance. However, excessive Rb loading may lead to surface restructuring or occupation of active sites, thereby reducing the concentration of $O_V$. The observed variations in the BE and distribution of O 1*s* further confirm the electronic interactions between Rb and the metal-oxide framework.

The adsorption and activation of $CO_2$ are crucial factors influencing the catalytic performance of CuZnFe and Rb-modified CuZnFe catalysts in $CO_2$ hydrogenation reactions. To assess the adsorption properties, $CO_2$ temperature-programmed desorption ($CO_2$-TPD) measurements were performed, as shown in Fig. 11. The desorption profiles (Fig. 11a) reveal three distinct temperature regions corresponding to different types of basic sites: the low-temperature region (50–300 °C), attributed to weak basic sites ($CO_2$ adsorption on hydroxyl groups); the medium-temperature region (300–570 °C), associated with moderate basic sites (oxygen vacancies or surface defects), observed mostly for the unmodified CuZnFe catalyst; the high-temperature region (above 570 °C), assigned to strong basic sites (coordination-unsaturated $O^{2-}$ species). The medium-temperature $CO_2$ desorption feature (300–570 °C) is most intense for the unmodified CuZnFe catalyst, indicating the presence of moderate basic sites related to oxygen vacancies and surface defects. After Rb addition, this peak decreases substantially but does not vanish entirely, reflecting partial neutralization or redistribution of these sites. The integrated $CO_2$ desorption values in Fig. 11(b), therefore, include residual contributions from this region for the Rb-modified catalysts, in agreement with the TPD profiles. The $CO_2$-TPD results show significant variations in $CO_2$ adsorption capacity with increasing Rb content. The unmodified CuZnFe catalyst exhibits moderate $CO_2$ desorption, with a prominent peak at 471.8 °C, indicating the presence of moderate basic sites. The incorporation of 2% Rb enhances $CO_2$ adsorption, particularly in the high-temperature range (675.8 °C), suggesting an increase in oxygen vacancies that facilitate $CO_2$ activation. Interestingly, the 4%Rb/CuZnFe catalyst exhibits a shift in the high-temperature desorption peak to a slightly lower temperature (663.8 °C), indicating the presence of relatively weaker basic

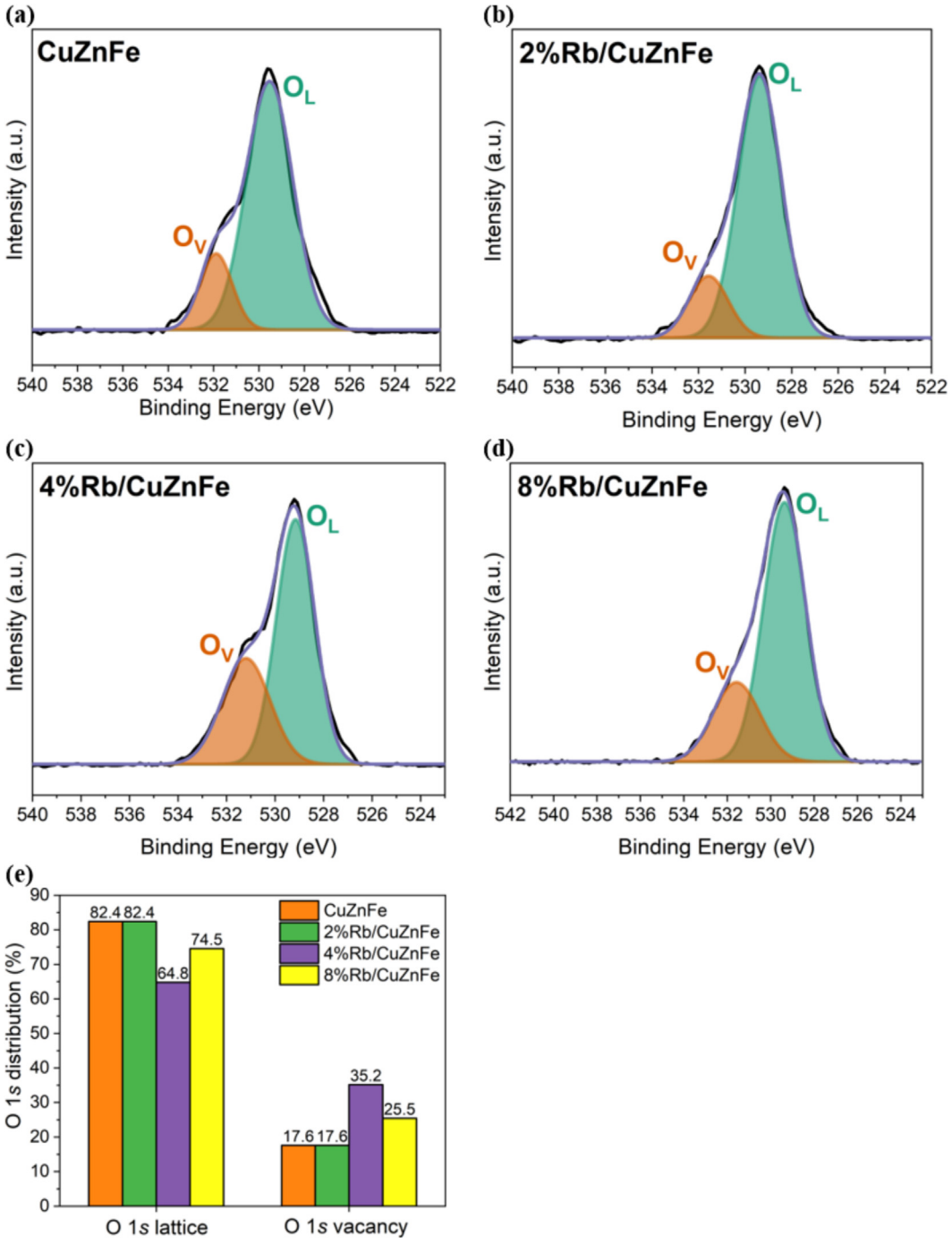


**Fig. 10.** Deconvoluted O 1*s* XPS spectra of (a) CuZnFe, (b) 2%Rb/CuZnFe, (c) 4%Rb/CuZnFe, and (d) 8%Rb/CuZnFe. (e) O 1*s* distribution.

sites. However, its total $CO_2$ adsorption capacity is slightly higher than that of the 2%Rb/CuZnFe catalyst, suggesting that modifications in the surface composition influence basicity and catalytic performance. The 8%Rb/CuZnFe catalyst exhibits the highest total $CO_2$ desorption, with a dominant high-temperature peak at 697.0 °C, confirming the formation of highly stable and strong basic sites. These strong sites, attributed to coordination-unsaturated $O^{2-}$ species, are particularly crucial for $CO_2$ activation and hydrogenation. However, an excessive number of strong basic sites may lead to over-adsorption of $CO_2$, potentially limiting catalytic efficiency due to restricted site availability and increased formation of side products. The quantitative $CO_2$ desorption data (Fig. 11b) further confirm these trends. The 2%Rb/CuZnFe catalyst shows a significant increase in total $CO_2$ adsorption compared to unmodified CuZnFe, with a balanced distribution of weak and moderate basic sites. The 4%Rb/CuZnFe catalyst, while exhibiting slightly higher total $CO_2$ adsorption, displays an increased proportion of strong basic sites, which may enhance selective $CO_2$ hydrogenation. In contrast, the 8%Rb/CuZnFe catalyst shows the highest total basicity, primarily due to the abundance of strong basic sites, which may not only enhance $CO_2$ activation but also pose selectivity challenges. The $CO_2$-TPD results demonstrate that Rb incorporation significantly modifies the basic properties of CuZnFe-based catalysts, with moderate Rb loading (2–4 wt%) providing an opti-

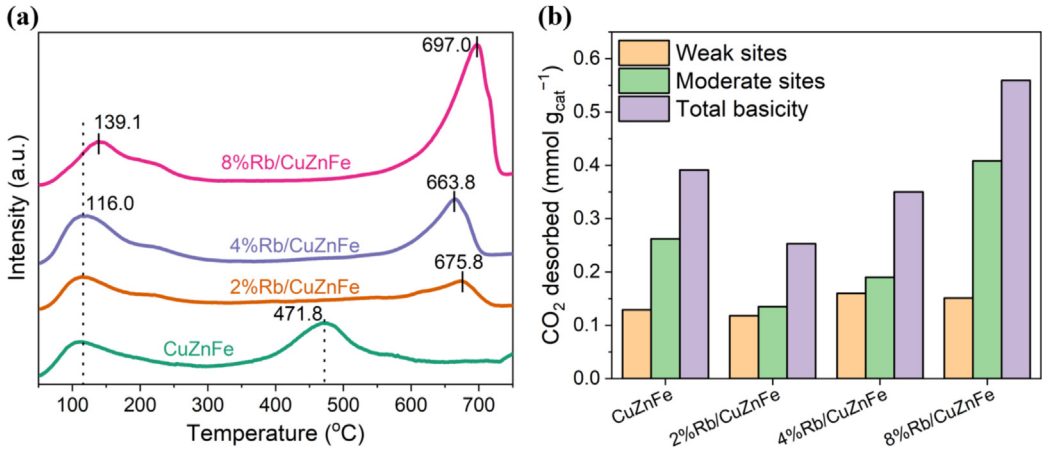


**Fig. 11.** The (a) $CO_2$-TPD and (b) $CO_2$ desorption results for the CuZnFe and *x*Rb/CuZnFe catalysts.

mal balance between weak and strong basic sites. While the 8%Rb/CuZnFe catalyst exhibits the highest basicity, excessive $CO_2$ adsorption may negatively impact selectivity in $CO_2$ hydrogenation reactions. These findings emphasize the importance of optimizing Rb content to achieve the best catalytic performance by carefully balancing $CO_2$ adsorption strength and active site availability.

The reaction mechanism of $CO_2$ hydrogenation over the 4%Rb/CuZnFe catalyst, as illustrated in Figs. S8, S9, proceeds via two primary pathways: the formate pathway and the CO insertion pathway, both of which are confirmed by in situ DRIFTS analysis presented in Fig. 12. The prominent infrared (IR) absorption band in the range of 2400–2200 $cm^{-1}$ can be attributed to the presence of gaseous $CO_2$ [39]. The reaction begins with $CO_2$ activation on the catalyst surface, forming $CO_3^*$ and $HCO^*$ species, as confirmed by the absorption bands at 1628 and 1511 $cm^{-1}$ in Fig. 12(c). The presence of intense gaseous CO signals at 2112 and 2179 $cm^{-1}$

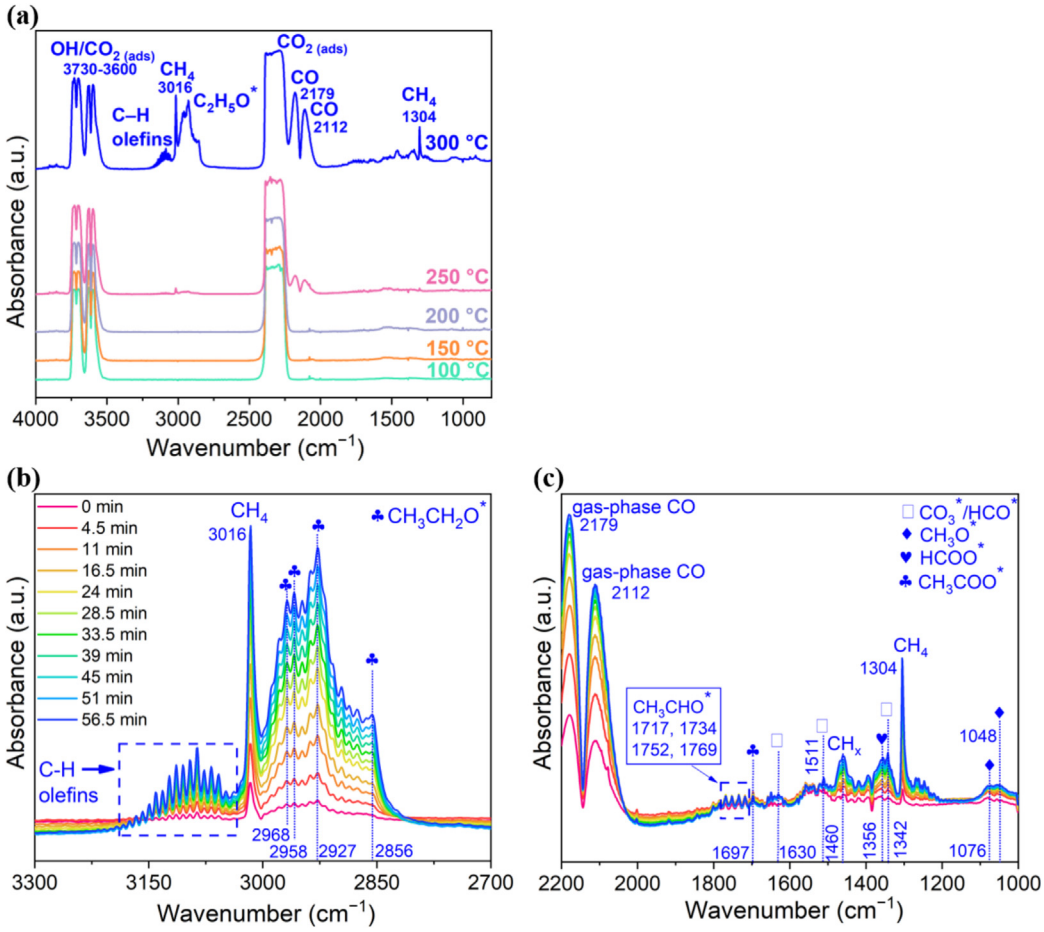


**Fig. 12.** In situ DRIFT spectra of surface species on the 4%Rb/CuZnFe catalyst during $CO_2$ hydrogenation ($H_2/CO_2$ = 3/1, P = 20 bar). (a) Spectra at different reaction temperatures (100–300 °C). (b, c) Time-resolved spectra at 300 °C.

indicates that the RWGS reaction proceeds rapidly at elevated temperatures (250–300 °C), facilitating the reduction of $CO_2$ to CO. This reaction is essential for further carbon chain growth, as CO acts as a key reactant in both hydrocarbon and oxygenate formation. The role of Rb promotion is particularly significant, as it increases surface alkalinity and enhances the adsorption of $CO_2$, stabilizing crucial intermediates such as HCO* and $CO_3$*.

In the formate pathway, $CO_2$ undergoes sequential hydrogenation to form HCOO* and $CH_3O$* species, as evidenced by the characteristic bands at 1356, 1076, and 1048 $cm^{-1}$ in Fig. 12(c). The presence of methoxy species is a critical step toward methanol formation, while the formation of $CH_3CH_2O$* species at 2968, 2958, 2927, and 2856 $cm^{-1}$ suggests that C–C coupling is facilitated under the reaction conditions [14,36]. Given that the ethanol formation rate significantly exceeded that of methanol, as confirmed by micro-GC and GC-MS (mass spectrometry) analyses, and considering the potential overlap of $CH_3CH_2O$* and $CH_2O$* bands in the region of 2940–2980 $cm^{-1}$, the features observed in Fig. 12(b) are confidently attributed to $CH_3CH_2O$*, a key intermediate in ethanol synthesis [27,29,40]. The progressive increase in their intensity with temperature and reaction time further supports a pathway involving the OHCCHO* intermediate, which undergoes subsequent hydrogenation to yield ethanol [41]. The Rb-modified CuZn sites enhance the stabilization of these intermediates, promoting ethanol selectivity over methanation.

The CO insertion pathway represents an alternative route for $C_{2+}$ oxygenate formation, in which CO reacts with Fe-based sites, leading to the formation of $FeC_x$ or chemisorbed CO species. Although the characterization of the spent catalyst was not conducted in this study, we acknowledge that $FeC_x$ species may be formed under reaction conditions and contribute to C–C coupling and CO insertion. This is consistent with previously reported systems [14,15,42]. The formation of $CH_3CHO$* and $CH_3CH_2O$* intermediates in our DRIFTS spectra may indirectly support the involvement of such species. The in situ DRIFTS spectra in Fig. 12 (c) reveal the presence of $CH_3CHO$* bands at 1717, 1734, 1752, and 1769 $cm^{-1}$, confirming that CO insertion leads to aldehyde formation. The subsequent hydrogenation of acetaldehyde results in ethanol formation, while further condensation or oxidation pathways can generate higher oxygenates such as acetone, butanoic acid, and acetic acid, as depicted in Fig. S9. The presence of additional carbonate species and methoxy/formate species further supports the idea that Rb plays a role in stabilizing these intermediates, preventing over-hydrogenation to methane.

The DRIFTS spectra also indicate competing pathways, including methanation and hydrocarbon (olefins) formation, particularly at higher temperatures. The peaks at 3016 and 1304 $cm^{-1}$ in Fig. 12 (a), attributed to $CH_4$, suggest that methane formation becomes more pronounced with increasing temperature or reaction time [39]. This is further supported by the presence of $CH_x$-related bands at 1460 $cm^{-1}$ in Fig. 12(c), indicating that a portion of the $CO_2$-derived CO undergoes complete hydrogenation rather than C–C coupling. Additionally, the detection of ethane and ethylene (Fig. 4) indicates that a fraction of CO intermediates undergoes Fischer-Tropsch pathways, resulting in hydrocarbon formation. This is further supported by the presence of the region of 3190–3030 $cm^{-1}$ in IR bands, which are characteristics of C–H stretching vibrations in olefins [43].

The promotional effect of Rb is strongly dependent on its loading, and the in situ DRIFTS results clearly demonstrate that 4% Rb provides the most favourable surface environment for ethanol formation. For the 2%Rb/CuZnFe catalyst, only weak or negligible bands related to ethanol-forming intermediates ($CH_3CH_2O$*, $CH_3CHO$*, and $CH_3COO$*) were detected at 300 °C (Fig. S10), and although they appeared at 350 °C, their intensity remained significantly lower than that observed for the 4% Rb catalyst. The spectra were dominated by CO* and $CH_4$ signals, together with features attributable to formates/carbonates (~1356, 1342 $cm^{-1}$), indicating that this catalyst preferentially promotes RWGS and methanation rather than selective $C_2$ oxygenate formation. In contrast, the 8% Rb/CuZnFe catalyst showed (Fig. S11) detectable $CH_3CH_2O$*-type bands (2968, 2958, 2927, and 2856 $cm^{-1}$), but with much lower intensity than that for the 4% Rb sample, while methane and olefin-related signals were markedly enhanced, again suggesting the promotion of RWGS and Fischer-Tropsch-type reactions rather than ethanol synthesis. The 4%Rb/CuZnFe catalyst exhibited the strongest and most stable $CH_3CH_2O$* bands already at 300 °C, confirming that this loading provides the optimal balance among electronic promotion, oxygen-vacancy creation, Cu dispersion, and Cu-Fe/Cu-Zn interfacial synergy, thereby stabilizing key $C_2$ intermediates and leading to superior ethanol selectivity and activity. The reaction mechanism over *x*Rb/CuZnFe is governed by a delicate balance of $CO_2$ activation, RWGS, C–C coupling, and hydrogenation, where moderate Rb loading enhances $CO_2$ adsorption and stabilizes key intermediates, directing selectivity toward ethanol and higher oxygenates instead of methane.

## 4. Conclusions

The 4 wt%Rb/CuZnFe catalyst shows excellent performance in $CO_2$ hydrogenation, delivering 4.4 mmol $g_{cat}^{-1}$ $h^{-1}$ ethanol STY with 48.8% selectivity in the gas phase, while the condensed liquid fraction reaches up to 85.3% $C_{2+}$OH selectivity, highlighting its remarkable capability for HA formation. The superior performance is attributed to the synergistic effects of electronic promotion, increased oxygen-vacancy concentration, and enhanced Cu-Fe and Cu-Zn interfacial interactions, supported by the preserved crystallinity and adequate pore structure for mass transport. These combined properties improve $CO_2$ activation and stabilize key reaction intermediates, leading to significantly higher activity than the other catalysts. Moreover, optimizing Rb content enhances Cu stability and minimizes leaching, highlighting the importance of precise Rb loading for improved catalytic performance in the $CO_2$ hydrogenation reaction to HA. The comprehensive physicochemical characterization reveals structural modifications upon Rb addition, indicating its dual role as both an electronic promoter and a structural modifier by influencing particle morphology, elemental distribution, and potential phase segregation. Ethanol and HA formation follow a multi-step pathway involving $CO_2$ activation, CO formation (RWGS), formate/methoxy intermediates, CO insertion, and ethoxide-mediated chain growth. Moderate Rb loading enhances $CO_2$ adsorption and stabilizes key intermediates, steering selectivity toward ethanol and higher oxygenates instead of methanol. This study offers valuable insights into the rational design and optimization of *x*Rb/CuZnFe catalysts for the thermocatalytic conversion of $CO_2$ into ethanol and HA. The catalyst maintained stable activity and ethanol selectivity during 16–19 h of continuous on-stream operation, with no indication of rapid deactivation. Longer tests (>100 h) are planned to evaluate long-term stability and will be presented in future work.

## CRediT authorship contribution statement

**Andrii Kostyniuk:** Writing – review & editing, Writing – original draft, Visualization, Validation, Software, Project administration, Methodology, Investigation, Formal analysis, Data curation, Conceptualization. **Stanislav Yakushkin:** Data curation, Investigation, Visualization, Writing – review & editing. **Blaž Likozar:** Writing – review & editing, Supervision, Resources, Project administration.

## Declaration of competing interest

The authors declare that they have no known competing financial interests or personal relationships that could have appeared to influence the work reported in this paper.

## Acknowledgments

This project has received funding from the European Union's Horizon Europe research and innovation programme under Grant Agreement No. 101214604 (CERNET project). The authors express their gratitude for the financial support provided by the Slovenian Research Agency (ARIS) through the research Grant J7-4638 (Unlocking the selective catalytic conversion processes of CO2 to ethanol – UliSess). The authors would also like to extend their thanks to Urška Kavčič for conducting N2 physisorption measurements, Dr. Anže Prašnikar for performing SEM analysis, Mr. Edi Kranjc for conducting XRD analysis and Dr. Goran Dražić for the assistance in TEM. The authors express their gratitude to Dr. Janez Kovač for conducting the XPS measurements.

## Appendix A. Supplementary material

Supplementary data to this article can be found online at https://doi.org/10.1016/j.jechem.2026.01.005.

## References

[1] J. Ye, N. Dimitratos, L.M. Rossi, N. Thonemann, A.M. Beale, R. Wojcieszak, Science 387 (2025) eadn9388.
[2] A. Kostyniuk, B. Likozar, Chem. Eng. J. 503 (2025) 158467.
[3] G. Tian, Z. Li, C. Zhang, X. Liu, X. Fan, K. Shen, H. Meng, N. Wang, H. Xiong, M. Zhao, X. Liang, L. Luo, L. Zhang, B. Yan, X. Chen, H.J. Peng, F. Wei, Nat. Commun. 15 (2024) 3037.
[4] X. Li, L. Li, X. Chu, X. Liu, G. Chen, Q. Guo, Z. Zhang, M. Wang, S. Wang, A. Tahn, Y. Sun, X. Feng, Nat. Commun. 15 (2024) 5639.
[5] A. Kostyniuk, D. Bajec, B. Likozar, Green Chem. 22 (2020) 753–765.
[6] C. Wang, J. Zhang, G. Qin, L. Wang, E. Zuidema, Q. Yang, S. Dang, C. Yang, J. Xiao, X. Meng, C. Mesters, F.S. Xiao, Chem 6 (2020) 646–657.
[7] C. Yang, R. Mu, G. Wang, J. Song, H. Tian, Z.J. Zhao, J. Gong, Chem. Sci. 10 (2019) 3161–3167.
[8] C. Zhou, A. Aitbekova, G. Liccardo, J. Oh, M. Stone, E.J. McShane, B. Werghi, S. Nathan, C. Song, J. Ciston, K. Bustillo, A.S. Hoffman, J. Hong, J. Perez-Aguilar, S. Bare, M. Cargnello, Angew. Chemie Int. Ed. 63 (2024) e202406761.
[9] S. Ji, F. Hong, D. Mao, Q. Guo, J. Yu, Chem. Eng. J. 495 (2024) 153633.
[10] S. Bai, Q. Shao, P. Wang, Q. Dai, X. Wang, X. Huang, J. Am. Chem. Soc. 139 (2017) 6827–6830.
[11] Y. Lou, F. Jiang, W. Zhu, L. Wang, T. Yao, S. Wang, B. Yang, B. Yang, Y. Zhu, X. Liu, Appl. Catal. B Environ. 291 (2021) 120122.
[12] L. Liu, J. Liu, G. Li, X. Shi, J. Yin, S. Zheng, K. Yung, H. Bin Yang, T. Woon, B. Lo, Angew. Chemie - Int. Ed. 64 (2025) e202422744.
[13] C.C. Tran, S. Kaliaguine, Chem. Eng. J. 496 (2024) 153636.
[14] P. Du, A. Ait El Fakir, S. Zhao, N.H.M. Dostagir, H. Pan, K.W. Ting, S. Mine, Y. Qian, K. Shimizu, T. Toyao, Chem. Sci. 15 (2024) 15925–15934.
[15] D. Xu, M. Ding, X. Hong, G. Liu, S.C.E. Tsang, ACS Catal. 10 (2020) 5250–5260.
[16] C. Yang, B. Wang, Y. Wen, M. Fan, Y. Jia, S. Zhou, W. Huang, Fuel 327 (2022) 125055.
[17] D. Xu, M. Ding, X. Hong, G. Liu, ACS Catal. 10 (2020) 14516–14526.
[18] S. Zhou, Y. Wen, B. Wang, M. Fan, L. Ren, Z. Cui, W. Huang, J. Li, J. Guo, Chem. Eng. J. 487 (2024) 150425.
[19] Y. Wang, W. Wang, R. He, M. Li, J. Zhang, F. Cao, J. Liu, S. Lin, X. Gao, G. Yang, M. Wang, T. Xing, T. Liu, Q. Liu, H. Hu, N. Tsubaki, M. Wu, Angew. Chemie 62 (2023) e202311786.
[20] Z. Si, L. Wang, Y. Han, J. Yu, Q. Ge, C. Zeng, J. Sun, ACS Sustain. Chem. Eng. 10 (2022) 14972–14979.
[21] G. Zhang, G. Fan, L. Zheng, F. Li, ACS Appl. Mater. Interfaces 14 (2022) 35569–35580.
[22] K. He, Y. Li, Z. Li, J. Chen, L. Tan, T. Qiu, X.G. Li, X. Ma, C. Dai, Chem. Eng. J. 501 (2024) 157608.
[23] W. Xiang, S. Yasuda, M. Tonooka, W. Yang, K. Tsukamoto, G. Liu, G. Yang, W. Gao, N. Tsubaki, Appl. Catal. B Environ. 369 (2025) 125157.
[24] S. Zhang, Z. Wu, X. Liu, Z. Shao, L. Xia, L. Zhong, H. Wang, Y. Sun, Appl. Catal. B Environ. 293 (2021) 120207.
[25] A. Kostyniuk, B. Likozar, Chem. Eng. J. 520 (2025) 166135.
[26] Y. Wang, K. Wang, B. Zhang, X. Peng, X. Gao, G. Yang, H. Hu, M. Wu, N. Tsubaki, ACS Catal. 11 (2021) 11742–11753.
[27] L. Ding, T. Shi, J. Gu, Y. Cui, Z. Zhang, C. Yang, T. Chen, M. Lin, P. Wang, N. Xue, L. Peng, X. Guo, Y. Zhu, Z. Chen, W. Ding, Chem 6 (2020) 2673–2689.
[28] Y. Wang, X. Zhang, X. Hong, G. Liu, ACS Sustain. Chem. Eng. 10 (2022) 8980–8987.
[29] D. Xu, H. Yang, X. Hong, G. Liu, S.C. Edman Tsang, ACS Catal. 11 (2021) 8978–8984.
[30] H. Guo, S. Li, F. Peng, H. Zhang, L. Xiong, C. Huang, C. Wang, X. Chen, Catal. Letters 145 (2015) 620–630.
[31] S. Santanta, M.T.M. Koper, H.M. Alisson, L.H. Vieira, E.M. Assaf, M. Assaf, J.F. Gomes, Appl. Catal. B, Environ. 324 (2023) 122221.
[32] M. Takagawa, A. Okamoto, H. Fujimura, Y. Izawa, H. Arakawa, Stud. Surf. Sci. Catal. 114 (1998) 525–528.
[33] A. Kostyniuk, D. Bajec, P. Djinović, B. Likozar, Chem. Eng. J. 394 (2020) 124945.
[34] X. Hu, C. Ding, C. Chen, Y. Yang, X. Zhang, X. Li, B. Chen, N. Wang, Appl. Catal. B Environ. 377 (2025) 125515.
[35] Y. Ge, A.J. Martín, M. Suvarna, T. Zou, F. Krumeich, J. Pérez-Ramírez, Appl. Catal. B Environ. Energy 378 (2025) 125578.
[36] Y. Wang, Y. Zhou, X. Zhang, M. Wang, T. Liu, J. Wei, G. Zhang, X. Hong, G. Liu, Appl. Catal. B Environ. 345 (2024) 123691.
[37] S. Gu, Z. Yang, J. Ding, J. Li, L. Wang, H. Wan, G. Guan, Appl. Catal. A. Gen. 704 (2025) 120375.
[38] M. Irshad, H. Jo, S. Ahmed, W. Yoon, S. Ki, H. Chun, J. Kim, Appl. Catal. B Environ. Energy 365 (2025) 124978.
[39] S.S. Bibi, H. Jo, J.R. Sugiarto, S. Ahmed, M. Irshad, W. Yoon, J. Kim, J. Energy Chem. 108 (2025) 769–784.
[40] J.V. Ochoa, C. Trevisanut, J.M.M. Millet, G. Busca, F. Cavani, J. Phys. Chem. C 117 (2013) 23908–23918.
[41] X. Wang, P.J. Ramírez, W. Liao, J.A. Rodriguez, P. Liu, J. Am. Chem. Soc. 143 (2021) 13103–13112.
[42] T. Liu, D. Xu, M. Song, X. Hong, G. Liu, ACS Catal. 13 (2023) 4667–4674.
[43] L. Zhang, Y. Dang, X. Zhou, P. Gao, A. Petrus van Bavel, H. Wang, S. Li, L. Shi, Y. Yang, E.I. Vovk, Y. Gao, Y. Sun, Innovation 2 (2021) 100170.